Two-Dimensional Microdischarge Jet Array in Air: Characterization and Inactivation of Virus

A Thesis
SUBMITTED TO THE FACULTY OF
UNIVERSITY OF MINNESOTA
BY

Gaurav Nayak

IN PARTIAL FULFILLMENT OF THE REQUIREMENTS
FOR THE DEGREE OF
MASTER OF SCIENCE

Adviser: Dr. Peter J. Bruggeman

June 2016

Acknowledgements

Firstly, I would like to express my sincere gratitude to my adviser, Dr. Peter J. Bruggeman for his continuous and unfading support of my Master's study and research, for his patience, guidance and immense knowledge. His comments and critical analysis of my work have been the greatest source of improvement in my research. His door was always open whenever I ran into some issues, and he would always come up with the best of solutions. I could not have imagined having a better advisor for my Master's work.

I would like to thank Dr. Sagar M. Goyal from the College of Veterinary Medicine, University of Minnesota, with whom I collaborated for virus work. He provided us with all the Lab facilities required for this work. The meetings with him were particularly helpful in advancing my research in the right direction. I would also like to thank Dr. Uwe Kortshagen for his insightful comments, but also for the hard questions which helped me widen my research perspective. Dr. Goyal and Dr. Kortshagen served as the committee members of my Master's thesis defense.

I would like to thank PhD Student, Hamada Aboubakr, with whom I did all the virus measurements. I learnt a great deal of biological analysis and techniques from him. The challenging discussions with him regarding explanation of results were very useful and enriching. I appreciate his eagerness and dedication to work even during the weekends and late at night.

I would like to thank Dr. Ronny Brandenburg from Leibniz Institute for Plasma Science and Technology, Griefswald, Germany for setting up the cross-correlation spectroscopic tool and for teaching me its know-how. I really appreciate the skype meetings with him, discussing the results in depth and clarifying my doubts.

I would like to thank Dr. João Santos Sousa from Laboratoire de Physique des Gaz et des Plasmas (LPGP), Paris, France for setting up the IR optical emission spectroscopic tool and helping me in the measurements. I am greatly thankful for his suggestions and comments.

I thank my fellow labmates, Santosh Kondeti, Paul Williams (ex-labmate) and Yuchen Luo for the stimulating discussions and their help. I also thank Paul's 3D printer for printing the prototype for my discharge electrode holder. I would like to thank visiting researchers, Yanjun Du and Gaku Oinuma for their help in measurements and great discussions. Yanjun also helped me in many of the formatting issues of this thesis work. I would like to thank our previous post-doctorate fellow, Dr. Shurik Yatom and research scholar, Dr. Urvashi Gangal for their useful comments and suggestions.

I would like to thank Dr. John Gorman for helping me in simulation work. I also thank PhD students, Harishankar Natesan and Priyatanu Roy for finding out the fault in my Comsol simulation.

My special thanks goes to ME Purchasing department, Julie Gilasevitch and Haewon Jun for placing orders for all the materials that I used in this research and making sure that I received them.

Last but not the least, I would like to thank my family, my parents and my brother (Saurav). Without them I would have never made it this far in life. They have been there for me every step of the way, have always loved me unconditionally, and have supported me through all of my tough decisions. And finally, I express my heartfelt gratitude to my dearest friend, Shubha for patiently being there, both mentally and spiritually, whenever I needed her.

Gaurav Nayak
22nd June, 2016

Dedication

This thesis is dedicated to my Parents, Mrs. Minakshi Kumari Dhal and Dr. Chandramani Nayak, for their endless love, support and encouragement.

Abstract

Cold atmospheric pressure plasmas (CAPs) have proven to be quite effective for surface disinfection, wound healing and even cancer treatment in recent years. One of the major societal challenges faced today is related to illness caused by food-borne bacteria and viruses, particularly in minimally processed, fresh or ready-to-eat foods. Gastroenteritis outbreaks, caused, for example, by the human Norovirus (NV) is a growing concern. Current used technologies seem not to be fully effective. In this work we focus on a possible solution based on CAP technology for surface disinfection.

Many discharge sources have been studied for disinfection and the two major challenges faced are the use of expensive noble gases (Ar/He) by many plasma sources and the difficulty to scale up the plasma devices. The efficacies of these devices also vary for different plasma sources, making it difficult to compare results from different research groups. Also, the interaction of plasma with the biological matter is not understood well, particularly for virus.

In this work, a two-dimensional array of micro dielectric barrier discharge is used to treat Feline Calicivirus (FCV), which is a surrogate for human Norovirus. The plasma source can be operated with an air flow rate (up to 94 standard liters per minute or slm).

The use of such discharge source also raises important scientific questions which are addressed in this work. These questions include the effect of gas flow rate on discharge properties and the production of reactive species responsible for virus inactivation and the underlying inactivation mechanism.

The plasma source is characterized via several diagnostic techniques such as current voltage measurements for electrical characterization and power measurements, optical emission spectroscopy (OES) to determine the gas temperature, cross-correlation spectroscopy (CCS) for microdischarge evolution and timescales, UV absorption spectroscopy to measure the O_3 density, absolute IR OES to measure the $O_2(a\ ^1\Delta_g)$ density and spectrophotometry to estimate the NO_x species density in aqueous medium. The results show that the discharge activity is strongly dependent on the gas flow rate particularly for gas residence times comparable to the applied high voltage cycle. The maximum difference in gas temperature at extreme plasma conditions do not exceed 50 K. The NO density is found to be reducing with smaller gas residence time. It is found that the reduced field E/N is dependent on the flow rate. The observed variation in the electric field is attributed to the change in the neutral gas densities. Both gas residence time and humidity have an impact on the space-charge distribution. The O_3 density is found to increase with increasing power density and saturates at higher power above 12 W, and the maximum density of 10^{22} m^{-3} is achieved at an intermediate flow rate of 20 slm. An optimal condition for $O_2(a\ ^1\Delta_g)$ generation is found that is a balance between power and gas residence. Higher specific energy leads to higher increase of $O_2(a\ ^1\Delta_g)$ density as compared to the O_3 density. It is also observed that the $O_2(a\ ^1\Delta_g)$ to O_3 density ratio could be controlled by the flow rate from 0.7 to almost 0.

The discharge source is used for FCV inactivation on surfaces (in the gas phase) and suspended in solution. Discharge power and treatment time have strong effect on the reduction in virus titer, while exposure distance or flow rate have negligible effect.

Humidity plays a major effect on FCV inactivation on surfaces, leading to complete inactivation (>4 $\log_{10}$) within 3 minutes of treatment. FCV inactivation can be explained by O_3 in gas phase and RNS in liquid phase. Nonetheless synergistic effects of ROS and RNS cannot be excluded, as similar production rates of O_3 and NO_x in discharge are determined. The $O_2(a\ ^1\Delta_g)$ density at conditions used for FCV treatment is at least 2 orders of magnitude lower than the ozone density and is not a dominant factor in the inactivation.

Table of Contents

List of Figures ix
Introduction 1
Chapter 1: Effect of flow on microdischarge dynamics and properties 5
1.1. Introduction 5
1.2. Experimental Setup and Methods 6
1.2.1. Plasma source and electrical characterization 6
1.2.2. Flow field model 8
1.2.3. Gas temperature measurement 8
1.2.4. Cross-correlation spectroscopy (CCS) 9
1.2.5. Electric field strength measurement 12
1.2.6. Electric field simulation in discharge gap 13
1.3. Results and Discussions 13
1.3.1. Flow field and gas residence time 13
1.3.2. Electrical characterization and gas temperature 14
1.3.3. Emission intensities as function of flow rate 18
1.3.4. Electric field strength as function of flow rate 22
1.3.5. Spatially resolved electric field distributions 24
1.4. Conclusion 27
Chapter 2: Ozone and Singlet Delta Oxygen production 29
2.1. Introduction 29
2.2. Experimental Setup and Methods 31
2.2.1. Plasma Discharge 31
2.2.2. Ozone density measurement 32
2.2.3. Absolute singlet delta oxygen (SDO) density measurement using IR OES 34
2.3. Results and Discussions 35
2.3.1. Effect of flow rate 35
2.3.2. Effect of discharge power 39
2.4. Conclusion 43
Chapter 3: Virus inactivation 44
3.1. Introduction 44
3.2. Experimental Setup and Methods 46
3.2.1. Plasma setup 46
3.2.2. Virus assay preparation and titration 48
3.2.3. FCV treatment 49
3.2.4. Time-delay measurements 50
3.2.5. pH measurements 50
3.2.6. O_3 *and* $O_2(a\ ^1\Delta_g)$ *densities* 50
3.2.7. Nitrite and nitrate concentrations 51
3.3. Results and Discussions 53
3.3.1. Gas-phase treatment 53
3.3.2. Liquid-phase treatment 59
3.4. Conclusion 63

Conclusion 65
Bibliography 68

List of Figures

Figure 1.1. Schematic and images of the two-dimensional microdischarge array in air including electrical circuit..... 7
Figure 1.2. Schematic of temporally-resolved emission measurements using Cross Correlation Spectroscopy (CCS)..... 11
Figure 1.3. Maximum velocities within the discharge geometry calculated using Ansys CFX for an air flow rate of 94 slm. Cross-section of 3 out of 30 calculated holes are shown, including the central hole. 14
Figure 1.4. Typical current and voltage waveforms of the 2D-microdischarges in air at 0 SLM and 94 SLM, with the current waveform at 94 SLM shifted by 0.5 A for clarity. The peak-to-peak amplitude of the applied voltage is identical (10.8 kV) for both the flow rates. 15
Figure 1.5. V-Q plots of discharges in air at 0 SLM and 94 SLM. The Lissajous figures shown are averaged over 40 periods by the oscilloscope. An image of the discharge is also included for both conditions. 17
Figure 1.6. Normalized rotational emission spectrum of the $N_2(C\ ^3\Pi_u \rightarrow B\ ^3\Pi_g)$ (0,0) transition at 337.1 nm for 0 and 94 slm at 5.7W with best fit. The spectrum for 0 SLM is shifted for clarity. 18
Figure 1.7. Temporal evolution of the light intensities of $N_2(C\ ^3\Pi_u \rightarrow B\ ^3\Pi_g)$ (0,0) at 337.1 nm (SPS), $N_2^+(B\ ^2\Sigma_u^+ \rightarrow X\ ^2\Sigma_g^+)$ (0,0) at 391.5 nm (FNS), $N_2(B\ ^3\Pi_g \rightarrow A\ ^3\Sigma_u^+)$ (0,0) at 585.4 nm (FPS) and $NO(A\ ^2\Sigma^+ \rightarrow X\ ^2\Pi)$ (0,0) at 272.4 nm (NO-γ) at (a) 0 SLM, (b) 1 SLM, (c) 5 SLM and (d) 94 SLM. The emission is recorded at the location of maximum intensity.. 20
Figure 1.8. Normalized temporal evolution of $N_2^+(B\ ^2\Sigma_u^+ \rightarrow X\ ^2\Sigma_g^+)$ (0, 0) at 391.5 nm (FNS) as a function of air flow rate. 21
Figure 1.9. Temporal evolution of $NO(A\ ^2\Sigma^+ \rightarrow X\ ^2\Pi)$ (0, 0) emission at (a) various air flow rates, and (b) various concentrations of NO added to 5 SLM air flow rate at 5.7W. 22
Figure 1.10. Temporal electric-field strength evolution obtained from the ratio of SPS and FNS transitions as a function of flow rate. The discharge power is kept constant at 5.7 W. (a) Positive half cycle and (b) negative half cycle. 23
Figure 1.11. Electric field simulation in the air gap using COMSOL Multiphysics 5.0 stationary electrostatics domain. 24
Figure 1.12. Spatio-temporal electric-field strength evolution obtained from the ratio of SPS and FNS transitions. The discharge power is kept constant at 5.7 W. (a) 0 SLM, positive half cycle, (b) 94 SLM, positive half cycle, (c) 0 SLM, negative half cycle, and (d) 94 SLM, negative half cycle. Note that the electric-field strength of one of the curves in (a) is reduced by a factor of 2. 25
Figure 2.1. Schematic of the ozone density measurement using UV absorption spectroscopy. 33
Figure 2.2. Schematic of the experimental setup used for the measurement of the absolute density of singlet delta oxygen $[O_2(a\ ^1\Delta_g)]$ by IR optical emission spectroscopy. 35

Figure 2.3. O_3 and $O_2(a\ ^1\Delta_g)$ absolute density with flow rates at a constant discharge power of 5.6 W. The flow rates for which the residence time equals one discharge cycle and the lifetime of $O_2(a\ ^1\Delta_g)$ in air is also indicated. 37
Figure 2.4. Time dependent species density obtained from a 0-D chemical kinetics model for conditions relevant for a micro-discharge in atmospheric pressure air [14]. 38
Figure 2.5. Production rate of O_3 and $O_2(a\ ^1\Delta_g)$ at 5.6W but variable air flow rates as a function of specific energy. 39
Figure 2.6. O_3 and $O_2(a\ ^1\Delta_g)$ density at varying powers at (a) 94 slm, (b) 28.3 slm and (c) 20 slm. 42
Figure 3.1. Schematic of the experimental setup used for FCV treatment. The platform on which the sample holder is mounted can be linearly displaced between 2mm and 40 cm from the discharge. 47
Figure 3.2. Nitrite and nitrate calibration curves. Nitrite standards (10-100 μM) after 30 minutes incubation at room temperature, and nitrate standards (10-500 μM) after 30 minutes incubation at 37^0C and 5% CO_2. The equation of the calibration curves and corresponding R-squared values are also shown. 52
Figure 3.3. Effects of discharge power and treatment time on FCV titer at 10 slm and 3 mm exposure distance. 54
Figure 3.4. Wet and dry treatment of FCV-coated steel discs at 14.5 W and 16.4 slm air flow rate 1 cm and 40 cm from the discharge as a function of treatment time. Discs are sprayed with distilled water every 2 minutes in between treatment starting at 0 minute. 55
Figure 3.5. Plasma treatment of wet FCV-coated steel discs at 14.5 W and 16.4 slm air flow rate for 5 minutes as a function of exposure distance from the discharge. Discs are sprayed with distilled water every 2 minutes in between treatment starting at the start of the plasma treatment. 56
Figure 3.6. Absolute ozone [O_3] density in the gas phase and HNO_3 density in the liquid phase through which the effluent is bubbled as a function of discharge power. 57
Figure 3.7. Nitrite (NO_2^-) and nitrate (NO_3^-) concentration measurement in DI water bubbler as a function of discharge treatment time. 58
Figure 3.8. Treatment of FCV in NaCl-Tris-EDTA (NTE) buffer solution as a function of time at 14.5 W, 16.4 slm, and 1 cm and 40 cm from the discharge. 60
Figure 3.9. pH measurement of treated distilled water (DI) and NTE solution at 1 cm and 40 cm from discharge as a function of time. 61
Figure 3.10. FCV inactivation of plasma treated distilled water at 14.5 W and 16.4 slm for 10 minutes and 1 cm exposure. Virus is added to the DI water and NTE before the treatment (Direct) and at various delay times after the treatment. Unexposed virus solution is the Control. 62
Figure 3.11. Nitrite (NO_2^-) and nitrate (NO_3^-) concentration measurement at 16.4 slm and 14.5 W. 63

Introduction

Plasmas are partly ionized gases comprising of various particles like photons, electrons, neutrals, positive and negative ions, atoms, radicals, reactive and excited species. They make up more than 99.9% of the visible matter in the universe. This includes the stars and the sun. Plasma discharges are also made in laboratories and these man-made plasmas have been used in many technological advancements. Nonetheless, they might be the less-known fourth state of matter to the majority of the public. Plasmas are enabling many high technological processes particularly in the semiconductor industry, ozonizers, and gas discharge lamps. More recently they are applied for disinfection and medical applications. These applications have become one of the fastest growing research areas because of the wide-scale research and primary focus on the application of plasmas for clinical treatment purposes [1].

In the context of plasma medicine, gas discharges generated at atmospheric pressure and near room temperature have proven to be very effective for surface treatment/disinfection, wound healing and sterilization, antisepsis and more recently, cancer cell treatment [2]. These discharges are more commonly known as CAPs (cold atmospheric pressure plasmas). The electric field produced in such discharges cause electron acceleration, and due to high collisional frequency with neutral gas molecules, it leads to ionization of the gases, dissociation of molecules and generation of high energy UV photons. Besides, a large amount of reactive species are also produced which make particularly air plasma chemistry highly complex. These species can react with the living cells or tissues and alter their properties, leading to pathogen inactivation under suitable

conditions. Different kinds of plasma sources have been developed for this application, of which the cold atmospheric pressure plasma jets (CAPPJs) and dielectric barrier discharges (DBDs) are the most commonly used. The treatment of biological cells or tissues can be performed in two distinctive approaches: direct and indirect. Direct treatment involves the flow of electrical current through the cells with the purpose of facilitating direct interaction (touching) between the plasma discharges with living cells, while for indirect treatments, the plasma does not contact the living cells and only the reactive species (and UV photons) are impinged upon them. In addition, plasma discharges can be used to treat aqueous solution to create plasma-activated water (PAW), which can subsequently be applied on surfaces or liquid volume to cause disinfection [3].

Most of these plasma biomedical devices are generated in noble gases (Ar/He) with a small admixture of air, O_2, N_2 and/or H_2O at flow rates of 1-2 slm and for a small target area often of the order of 1 mm^2. Plasma operation in ambient air without the necessity of a feed gas supply would be advantageous from the application point of view.

The presented work deals with a two-dimensional array of microdischarges which operates in laboratory-grade air at high flow rates up to 94 slm and with an active area of 2.5 by 2.5 cm^2 which allows for easier and larger area treatments. The discharge is also easy to scale up. The discharges are confined within the array geometry and the plasma effluent is blown on the substrate or liquid volumes. The source is thus intended for indirect treatment. Due to the current limiting feature of microdischarges generated in a dielectric barrier discharge (DBD) geometry, the gas temperature remains low (<50 K), which also makes it ideal for treatment of heat sensitive surfaces.

The motivation for the current work arises from the fact that food-borne bacteria and viruses (such as human Norovirus) particularly in minimally processed or fresh foods have been implicated in many outbreaks of gastroenteritis worldwide and are a real threat to public health. The goal of this work is to assess the specific plasma technology under consideration as an efficient inactivation method for virus and provide answers to some of the associated research goals like –

- What is the influence of the gas flow rate on the discharge properties of this particular plasma source?
- What are the effects of gas flow rates (and gas residence time) on plasma-generated species in air like ozone (O_3) and singlet delta oxygen ($O_2(a\ ^1\Delta_g)$) that are important for biological interactions?
- What are optimum conditions for virus inactivation?
- Which plasma-produced species are responsible for the virus inactivation?

The outline of this dissertation is as follows. Chapter 1 introduces the plasma source (microdischarge array) and deals with the electrical characterization and estimation of the gas temperature. Since the air-plasma chemistry is initiated or generated in a micro-discharge with a typical duration of the order of 10 ns, it is important to investigate the microdischarge evolution using highly time-resolved diagnostic tools. This investigation is performed with cross-correlation spectroscopy. We also performed electric field measurements. The key goal of this chapter is to assess the effect of gas flow rates and gas residence time on these parameters.

It has been previously reported that reactive oxygen species (ROS) play a major role in microbicidal activity [4-8], especially O_3 and $O_2(a\ ^1\Delta_g)$. In Chapter 2, the O_3 and $O_2(a\ ^1\Delta_g)$ generation in the two-dimensional array of micro-discharges in air is investigated. Many applications that rely on $O_2(a\ ^1\Delta_g)$ require sensitive diagnostics technique to measure, monitor and control its production in order to optimize the relevant processes. This chapter introduces the first attempt of its kind to experimentally determine the $O_2(a\ ^1\Delta_g)$ absolute density in an atmospheric pressure DBD in air using IR optical emission spectroscopy. The ozone density is also measured using UV absorption spectroscopy as it is one of the main quenchers of $O_2(a\ ^1\Delta_g)$ in air. The effects of flow rate on the production of these important species are discussed.

Chapter 3 introduces the microdischarge array reactor as an effective tool for inactivation of feline calicivirus (FCV), a surrogate for human Norovirus that is responsible for many outbreaks of gastroenteritis. The full study of the complete complex cocktail of reactive species generated by the discharge is out of the scope of this work, but the effect of most important species in inactivation (as mentioned in literature) like O_3, $O_2(a\ ^1\Delta_g)$, NO, NO_2, HNO_2 and HNO_3 [6, 9] are investigated in detail. Both the gas-phase and liquid-phase treatments of FCV are studied and the results are compared with previous works using similar DBD devices. The chapter deals with the effects of discharge power, treatment time, exposure distance and pH of the treated solution on FCV and presents an apparent optimal condition for virus inactivation.

Finally, the key findings and conclusions of this work are summarized.

Chapter 1: Effect of flow on microdischarge dynamics and properties [1]

1.1. Introduction

Many industrial applications such as surface treatment and processing require large area plasma sources. Particularly at atmospheric pressure it is extremely challenging to generate large volume stable discharges. A typical approach is the use of a dielectric barrier discharge (DBD) discharge. Sakai *et al* developed the first dielectric barrier microdischarge-integrated 2D array device that allows a fast gas throughput through the active discharge zone [10]. The gas flow is perpendicular to the electrode settings, which is unlike most of the plasma sources in which the flow is in between and parallel to the electrodes. In the work of Sakai *et al*, the effect of flow on the microdischarges has been studied using CCD images. Similar research has been recently performed by Höft et al., where the effect of flow on the discharge ignition on a volume micro-discharge has been studied [11]. The effect of flow on the discharge has not been investigated in detail to date. However a large amount of literature is available on utilizing DBDs to control or generate gas flow as reviewed by Moreau [12].

The effect of fast gas flow on the stability of a corona discharge in air has been studied by Akishev *et al* [13]. However, an experimental study of the time-resolved evolution and ignition of microdischarges with a small gas residence time have not been reported. The small residence time can have an impact on gas heating, pre-ionization and other

[1] This chapter described work that is collaboratively performed with Dr. Ronny Brandenburg from Leibniz Institute for Plasma Science and Technology, Greifswald, Germany. The TC SPC module is provided and installed by Dr. Brandenburg. All the spectroscopic measurements have been performed jointly with Yanjun Du.

remaining species produced by previous discharges. The present work is based on the investigation of the effect of gas residence time on the microdischarge evolution using highly time-resolved electrical and optical diagnostics.

This work comprises of the following: Section 1.2 introduces the plasma source, electrical characterization, modeling of the gas flow field through the discharge geometry, estimation of gas temperature, time-resolved cross-correlation spectroscopic (CCS) measurements, and determination of electric field strength. Section 1.3 presents the experimental results and their analysis. Finally the conclusions are presented in section 1.4.

1.2. Experimental Setup and Methods

1.2.1. Plasma source and electrical characterization

The plasma source is shown in Figure 1.1. The microdischarge array operates in air at atmospheric pressure. The electrode geometry manufactured by Kyocera Inc., Japan, consists of two unequal ultra-thin metal electrodes, nickel and gold, which are coated and separated by 500 μm thick layer of alumina (Al_2O_3). The thinner gold electrode is grounded and also the closest to detection. The multilayered electrode consists of 105 through-holes, arranged in a grid-like array and evenly distributed. Each hole has a diameter of 600 μm, in which the discharge is created. The coaxial-hollow discharge source is embedded in a homemade Polytetrafluoroethane holder attached to a polycarbonate tube to allow for an air flow and the electrical connections. The sinusoidal high voltage signal at 20 kHz is generated by an AC power source (PVM500) and applied to the electrode which is not exposed to the detection and imaging diagnostics to measure

the charge Q, the other electrode is grounded through a capacitor (C) of 82 nF which is much larger than the capacitance of the microdischarge array (≈ 70 pF). The electrical characteristics of the discharge are recorded using an oscilloscope (Tektronix DPO2024B, 200 MHz). The voltage at the anode (V) is measured by a high-voltage probe (Tektronix P6015A), while the voltage across the capacitor (V_C) is acquired using a passive probe (Tektronix TPP0200). The airflow through the source is controlled by a rotameter (200 SCFH Dwyer Inc.). All experiments have been performed either in ambient air with no flow or at different dry air flow rates up to 94 standard liters per minute (slm).

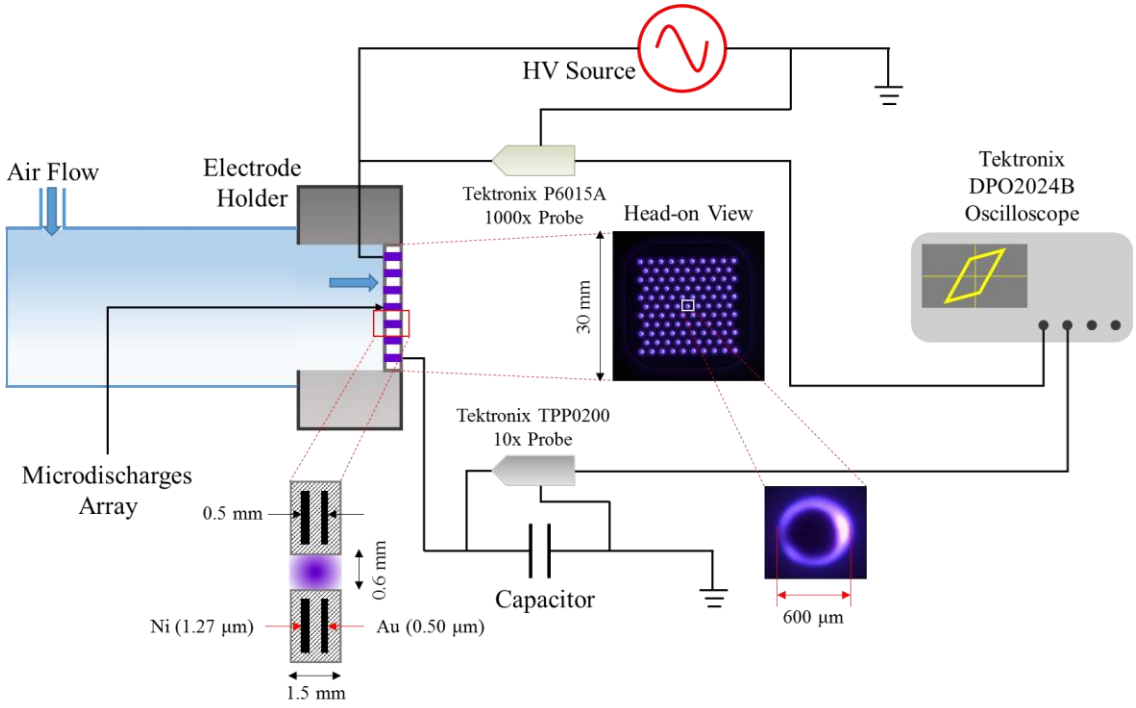

Figure 1.1. Schematic and images of the two-dimensional microdischarge array in air including electrical circuit.

The energy (E) dissipated by the plasma during one period of the high voltage cycle is determined from the voltage-charge plots recorded by the oscilloscope and multiplied

with the frequency (f) of the high voltage to determine the discharge power (P). The following equation is used for the analysis [14]:

$$P = \int (V - V_C) I dt = \int (V - V_C) dQ \tag{1.1}$$

where Q is the charge on the capacitor.

1.2.2. Flow field model

The flow field is simulated in Ansys CFX for 30 microdischarges spots, i.e. only a quarter of the plasma source is simulated in order to reduce calculation time. Triangular meshing is applied to the bulk gas, while inflation layers are provided at the edges where the most disturbance in the flow is expected. In total approximately 480,000 mesh nodes and 2 million mesh elements are utilized. The grid independence has been checked by using two different meshing methods with lower and the other with higher number of mesh elements. A shear stress transport model is used to include turbulence. The highest flow rate of 94 slm used, leads to a Reynolds number in a single discharge geometry of 2743. As only $1/4^{th}$ of the flow geometry is modelled, symmetric boundary conditions are used at the axial cut-sections. For the inlet, the mass flow rate is assumed to be the constant parameter, while the outlet is treated as an entrainment with 0 Pa relative pressure. The fluid layers in contact with the wall surfaces are assumed to be stationary (no slip wall). A maximum of 100,000 iterations are used for convergence control with a residual target of 0.0001%.

1.2.3. Gas temperature measurement

It has been previously shown that the rotational temperature of the $N_2(C\ ^3\Pi_u \rightarrow B\ ^3\Pi_g)$ transition provides a good estimate of the gas temperature in air plasmas [15]. The time-

averaged $N_2(C\ ^3\Pi_u \rightarrow B\ ^3\Pi_g)$ (0,0) transition at 337.1 nm is recorded to determine the gas temperature. The spectra are recorded by a 1 m high-resolution monochromator (ARC AM-510) with an intensified CCD camera (Andor iDus) as detector. The measurement is performed in second order of the diffraction grating (1800 g/mm) to achieve a spectral resolution of 40 pm FWHM. The array of microdischarges is placed in front of the monochromator slit without any lenses. The spectrum consists of 20 randomly accumulated measurements each with 100 μs integration time. The obtained spectrum is fitted with a synthetic spectrum using Specair software [16] at various rotational temperatures, T_{rot} to achieve the best fit.

1.2.4. Cross-correlation spectroscopy (CCS)

To measure weak time resolved plasma emission of transient microdischarges generated by kHz voltages several accumulations are necessary requiring a highly reproducible discharge event. The jitter in discharge inception is a key challenge. However, when a correlation is made between two optical signals arising from the same source based on the time delay between the signal of interest and the total emission of the discharge event, jitter can be accounted for. This delay is a measure of the probability with which a discharge pulse evolves. Provided the discharge pulses are reproducible and the synchronizing signal detects the light pulse at the same moment, the recorded probability density function is proportional to the light intensity of the source [17]. Using this time-correlated single photon counting technique called cross-correlation spectroscopy, the microdischarge dynamics within a single hole is investigated on sub-ns timescale.

Figure 1.2 shows a schematic of the implementation of CCS for the measurements presented in this work. All CCS recorded emissions are line of sight integrated, which limits the measurement of the discharge generation along the length of the discharge geometry. The synchronizing or SYNC signal defines a relative timescale and is detected by a photomultiplier (Hamamatsu H5773-06) through an optical fiber. The optical or MAIN signal from a single microdischarge hole is imaged and magnified by an achromatic lens (Edmund Optics UV-NIR Triplet 90mm EFL) on the entrance slit of a monochromator (Jobin Yvon HR320). The spatial resolution of the measurement (with an entrance slit of 190 μm) equals 33 μm. The signal is detected by a highly sensitive photomultiplier (Hamamatsu H5773-04) operating in single-photon-counting mode (high gain) after spectral separation in the monochromator. The spectral resolution of the optical detection is 0.471 nm FWHM. The statistical averaging of the results and the determination of the correlation function are done by the time-correlated single-photon-counting (TC SPC) module (Becker and Hickl GmbH, SPC-530). This module basically consists of two constant fraction discriminators (CFDs) which select the electric pulses from the two signals. The main signal starts the voltage rise of the pulse in the time-to-amplitude converter (TAC), while the synchronizing signal terminates it, giving rise to a final voltage amplitude. The analog-to-digital converter (ADC) converts this amplitude into corresponding time channel which addresses a memory segment. The TAC-time window (coincidence interval) is 50 ns long and is divided into 4096 equal segments, which results into a temporal resolution of 12.2 ps. Additionally, one period of the voltage cycle (50 μs) is divided into 16 equal coarse time intervals and synchronized with

the phase of the applied voltage through a TTL reference signal. Time-correlated measurement results are accumulated simultaneously in these 16 memory segments, and intensities with similar spatio-temporal structures after normalization are analyzed. A detailed description of the principles of CCS applied for microdischarge studies can be found in [18].

The spatio-temporal distribution of the light intensities of the second positive system (SPS) of nitrogen – $N_2(C\ ^3\Pi_u \rightarrow B\ ^3\Pi_g)$ (0,0) at 337.1 nm, the first negative system (FNS) – $N_2^+(B\ ^2\Sigma_u^+ \rightarrow X\ ^2\Sigma_g^+)$ (0,0) at 391.5 nm, the first positive system (FPS) of nitrogen – $N_2(B\ ^3\Pi_g \rightarrow A\ ^3\Sigma_u^+)$ (0,0) at 585.4 nm and the NO-γ system – $NO(A\ ^2\Sigma^+ \rightarrow X\ ^2\Pi)$ (0,0) at 272.4 nm are investigated for the discharge operating with and without gas flow.

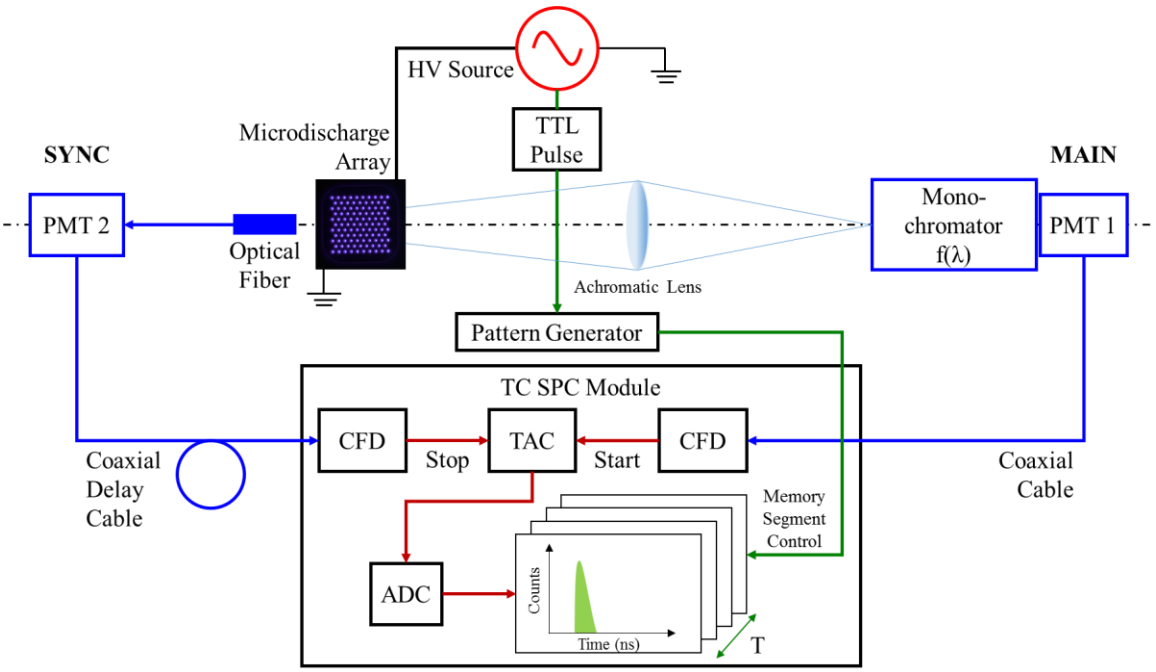

Figure 1.2. Schematic of temporally-resolved emission measurements using Cross Correlation Spectroscopy (CCS) [18].

1.2.5. Electric field strength measurement

The intensity ratio of FNS and SPS transitions, $R_{391/337}$ can be used to determine the electric field strength, if the N_2 molecules are excited dominantly from the ground state directly by the electron impact [17, 19]. It has been shown that these conditions are fulfilled for microdischarges in air. This intensity ratio depends on the reduced electric field strength (E/N) and can be written as [19]:

$$R_{391/337}\left(\frac{E}{N}, N_0\right) = \frac{I_B + \tau_{eff}^{B}\left(dI_B/dt\right)}{I_C + \tau_{eff}^{C}\left(dI_C/dt\right)} \tag{1.2}$$

where I_B and I_C are the FNS and SPS emission intensities, respectively. The effective life times, τ_{eff} of the two transitions are calculated from the respective radiative lifetimes (τ_0^B, τ_0^C), quenching rate constants and concentrations of nitrogen and oxygen. The values equal 0.562 ns and 0.045 ns for the $N_2(C)$ and the $N_2^+(B)$ states, respectively in atmospheric pressure air at room temperature [15].

Using CCS, the temporal evolution of the line integrated light intensities of SPS and FNS are recorded. The wavelength dependent sensitivity of the detection system is determined by a broadband laser-stabilized lamp (Energetiq EQ99) and corrected for. In addition, the spectral resolution of the optical system is 0.471 nm FWHM and the measured intensity is rescaled to the total band intensity considering the discrepancy between the measured intensity and the total band intensity through comparison with a synthetic rotational spectrum. A Savitzky-Golay smoothing of the recorded signal is performed (20 averaging points and 2nd order polynomial) to reduce the introduced noise by taking the time-derivative of this signal.

1.2.6. Electric field simulation in discharge gap

In order to estimate the electric field in the air gap within the discharge geometry, a stationary electrostatic 2D axisymmetric simulation without plasma is performed using Comsol Multiphysics 5.0. Only a single microdischarge geometry is considered. The electrode surfaces are treated as boundary with given potential and the fluid region is stretched in both directions (r and z) by 300 mm to neglect any influence of edge effects close to the edge of the computational domain on the E-field in the discharge gap. The materials are used from the Comsol materials library. A relative permittivity value of 9.1 is assigned to the dielectric (alumina) region. Triangular meshing with extremely fine element size is used. An electric potential of 10.8 kV (the same as experimental conditions) is applied to the top electrode, while the bottom one is grounded. The fluid-dielectric interface is assumed to have the same potential and no charge accumulation.

1.3. Results and Discussions

1.3.1. Flow field and gas residence time

The flow characteristics at 94 slm analyzed using Ansys in the central hole are shown in Figure 1.3. The gas velocity magnitude increases from 1.1 m/s in the undisturbed region upstream to around 74 m/s in the bulk of the discharge zone. This increase is consistent with the ratio of the cross section of the tube and discharge, equal to 53.6. The existing pressure difference of 3000 Pa and the expansion of the gas jet in the surrounding air reduces the gas velocity to 14 m/s 10 mm away from the discharge surface. The high velocity in the bulk region accounts for a very small residence time, t_{res} of 20 μs. The residence time in the boundary layer close to the dielectric surfaces is 50 μs which is the

same as the period of one voltage period, T. As discussed by Höft *et al.* [11], the residence time directly affects individual discharge events if t_{res} is smaller or equal to T. At 94 slm, t_{res} becomes 0.4 times T. However in the flow boundary layer with thickness approximately equal to 100 μm which is similar to the plasma emission zone (see further), t_{res} ~ T. Using t_{res} as the independent parameter, the effect of flow rate on the discharge evolution is discussed further.

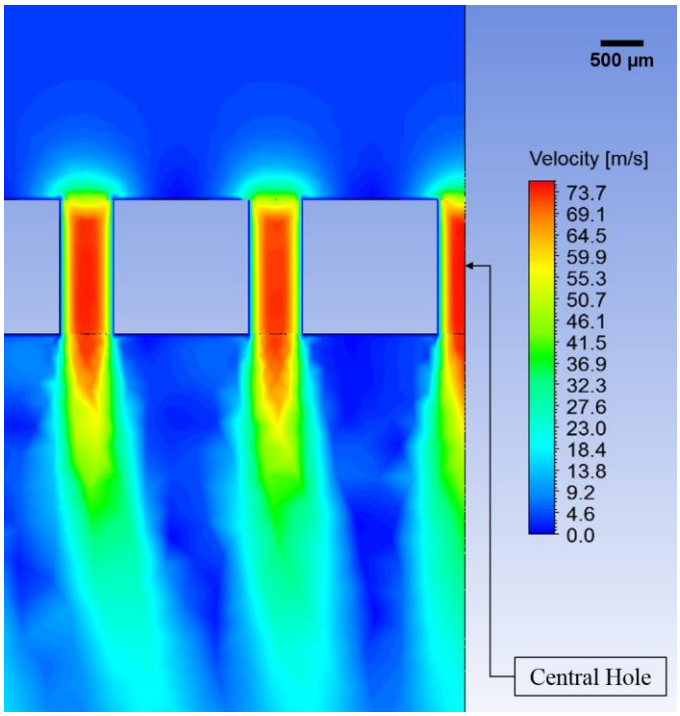

Figure 1.3. Maximum velocities within the discharge geometry calculated using Ansys CFX for an air flow rate of 94 slm. Cross-section of 3 out of 30 calculated holes are shown, including the central hole.

1.3.2. Electrical characterization and gas temperature

Figure 1.4 shows the voltage and current waveforms for the DBD driven by an AC high voltage cycle of 20 kHz and 10.8 kV_{p-p}. The measured current consists of a capacitive displacement current with a shift of about T/2 against the voltage and the current induced by microdischarges visible as the spikes. In each cycle, two time windows with discharge activities are registered. Multiple microdischarges are generated in each active window.

The duration of one microdischarge has an FWHM of ~10 ns. The influence of the gas residence time on these discharge characteristics is also depicted in Figure 1.4. A breakdown delay of around 2 μs is clearly visible with higher flow rate in the positive half of the cycle due to a higher breakdown voltage, which is in agreement to [11]. However, this is not observed in the negative half of the cycle. Comparing the time delay between the inceptions of microdischarges in a single high voltage cycle (~22.8 μs) to the t_{res} in the bulk region at 94 slm (20 μs) suggests that there is no accumulation of discharge products produced by previous discharge pulses. A reduction in accumulation of charged species and metastable species can increase the breakdown voltage. However, the boundary layers, close to the surface can still have a volume memory effect from the preceding discharge events due to a larger local t_{res}.

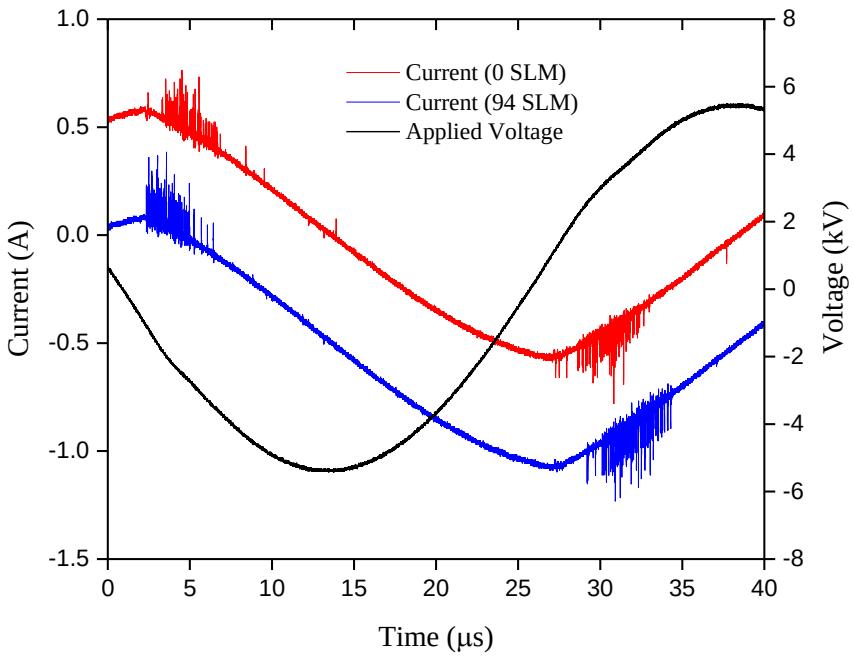

Figure 1.4. Typical current and voltage waveforms of the 2D-microdischarges in air at 0 SLM and 94 SLM, with the current waveform at 94 SLM shifted by 0.5 A for clarity. The peak-to-peak amplitude of the applied voltage is identical (10.8 kV) for both the flow rates.

The voltage-charge (V-Q) plots for both operating conditions are shown in Figure 1.5 along with the corresponding images of a single discharge hole. The area enclosed within the V-Q plot represents the energy dissipated by the plasma during one period of the voltage cycle [20]. The figures have been shifted with a value of ±0.5 kV for 0 and 94 slm respectively to enhance clarity. The slopes of the figure relate to the gap capacitance and the capacitance of the dielectric. For both the flow conditions, the difference in the slopes is 2.2% and 6.4%, with nominal values of 69.2 pF and 110 pF, respectively. The capacities might also be similar because of approximately same applied voltage and same coverage of surface by plasma. These figures differ significantly from the classical Lissajous plots with parallelogram structure reported in literature [20], with extended tails on either side of the curve. These tails define the dark periods or no discharge zones during part of the voltage waveform, which is consistent with the current and voltage waveforms in Figure 1.4. One major difference is that the V-Q plot for 94 slm is shifted to higher voltages, which might be due to the increased breakdown voltage at higher flow rate as discussed by Höft *et al.* [11]. Similar explanation can be provided for the larger extension of the tail in 94 slm as compared to 0 slm. The overall emission shown in the two images is very similar. But, significant differences are observed in the time evolution of emission intensities (see further).

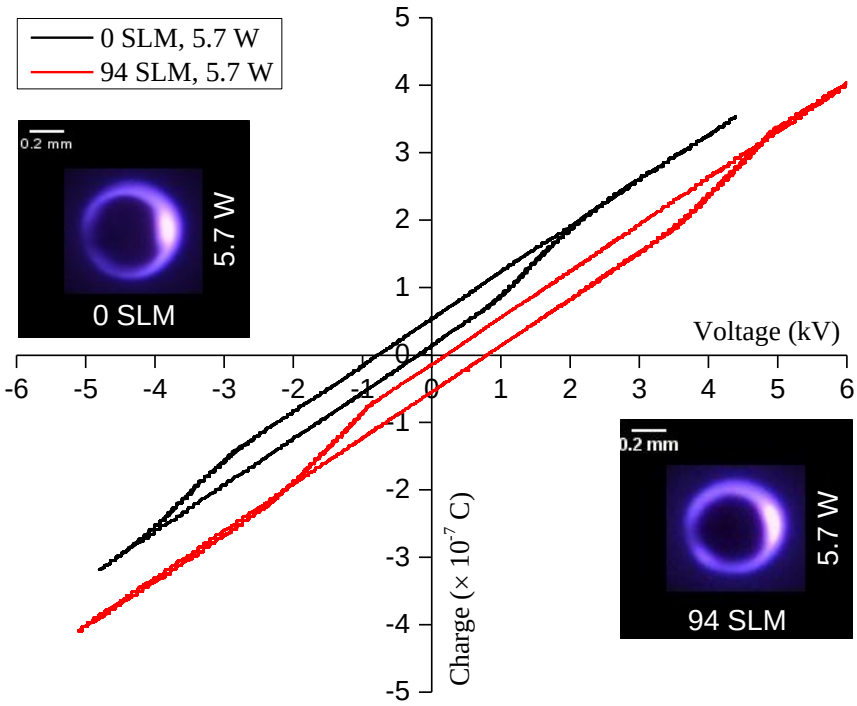

Figure 1.5. V-Q plots of discharges in air at 0 SLM and 94 SLM. The Lissajous figures shown are averaged over 40 periods by the oscilloscope. An image of the discharge is also included for both conditions.

The gas temperatures for 0 and 94 slm are measured using the method described in *Section 1.2.3*, and the N_2(*C*-*B*) (0,0) molecular band is shown in Figure 1.6. The gas temperature varies from 344±18 K to 300±15 K from no flow to 94 slm. The change in gas temperature is small and only leads to minor differences in neutral gas densities.

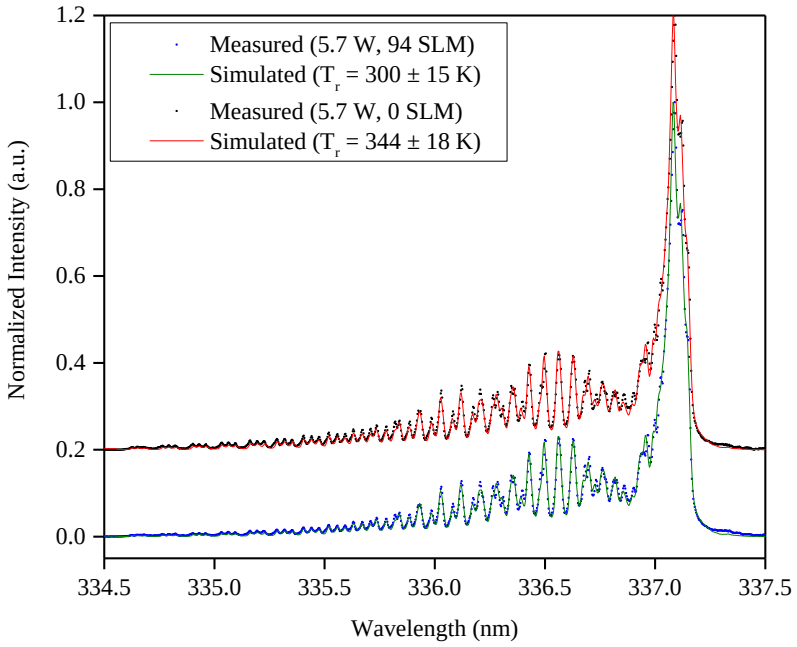

Figure 1.6. Normalized rotational emission spectrum of the $N_2(C\ ^3\Pi_u \rightarrow B\ ^3\Pi_g)$ (0,0) transition at 337.1 nm for 0 and 94 slm at 5.7W with best fit. The spectrum for 0 SLM is shifted for clarity.

1.3.3. Emission intensities as function of flow rate

Figure 1.7 shows the temporal evolution of the SPS, FNS, FPS and NO-γ transitions for 4 different flow rates at the location of maximum emission intensity, which is around 75 μm from the edge of the hole, within the discharge geometry. Comparing the width of a single microdischarge event to the FWHM of the emissions suggests that each plot represents a single microdischarge event in the central hole per half cycle. The FNS reaches its maximum earlier than the SPS in all cases. This is consistent with the high electron energy in the streamer phase required for the excitation of $N_2(X)$ to the $N_2^+(B)$ state (18.75 eV) [21] while the excitation energy for the $N_2(C)$ state is 11.0 eV [22]. After the maximum intensity is achieved, both SPS and FNS are shown to decay exponentially with time constants of 1.1 ns and 1.4 ns, respectively at 0 slm, and 1.0 ns and 1.2 ns, respectively at 94 slm. The large electron-neutral collision frequency causes fast

relaxation of the energy of energetic electrons responsible for the excitation of high energy excited states immediately after the discharge event [23]. The fast decay of the emission is further determined by collisional quenching of the excited states by N_2 and O_2 ground state molecules, thus, considerably smaller time constants than the radiative lifetimes (36.5 ns for $N_2(C)$ and 62.5 ns for $N_2^+(B)$) are obtained. Figure 1.8 shows the growth of the double-maximum structure in the FNS emission with increasing flow rate. This effect is more important with increasing distance from the hole-surface and is most likely due to the line of sight measurement of the emission. The first maximum is due to the fast cathode-directed streamer propagation, while the second maximum occurs when the streamer has reached the cathode, and electrons are accelerated towards the anode during the formation of a plasma filament [17]. The double maxima are not observed at the dielectric surface. This suggests that the filament is propagating in the bulk at a certain distance away from the surface, which is also known from other coplanar DBD arrangements [27]. In addition, with increasing flow rate, the FWHM of FNS emission broadens while the FWHM of the SPS emission becomes smaller.

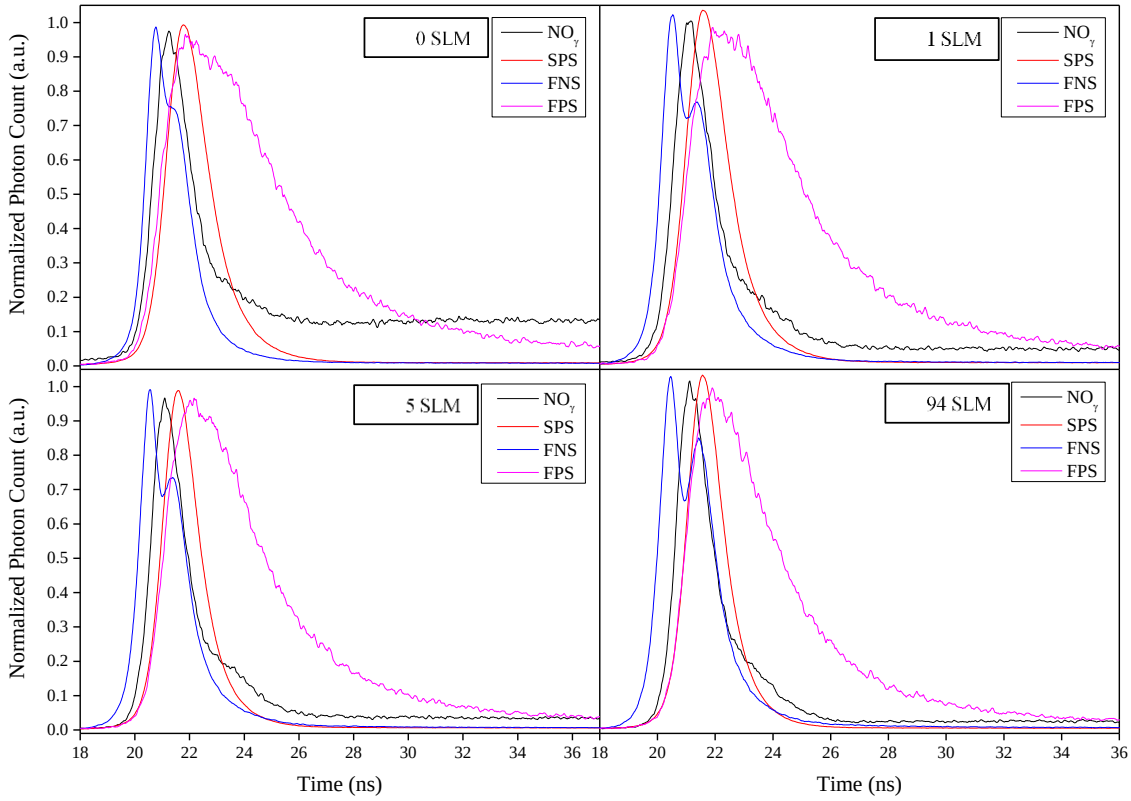

Figure 1.7. Temporal evolution of the light intensities of $N_2(C\ ^3\Pi_u \rightarrow B\ ^3\Pi_g)$ (0,0) at 337.1 nm (SPS), $N_2^+(B\ ^2\Sigma_u^+ \rightarrow X\ ^2\Sigma_g^+)$ (0,0) at 391.5 nm (FNS), $N_2(B\ ^3\Pi_g \rightarrow A\ ^3\Sigma_u^+)$ (0,0) at 585.4 nm (FPS) and NO($A\ ^2\Sigma^+ \rightarrow X\ ^2\Pi$) (0,0) at 272.4 nm (NO-γ) at (a) 0 SLM, (b) 1 SLM, (c) 5 SLM and (d) 94 SLM. The emission is recorded at the location of maximum intensity.

While the FNS and SPS follow the structure of a current pulse, strongly deviating behavior is found for the NO-γ and FPS emission. Both the NO-γ and FPS emissions prevail for more than 10 ns after the discharge. The emission intensity of the FPS is approximately 3 orders of magnitude lower than the emission intensity of the SPS. While initially, electron excitation from the ground state can play a role in the production of the $N_2(B)$ state, the radiative decay of the $N_2(C)$ state causes a delayed population of the $N_2(B)$ state. The lifetime of the metastable $N_2(A)$ state in air is determined by the collisional de-excitation of O_2 with quenching rates 2.5×10^{-12} cm^3s^{-1} [24] resulting in an $N_2(A)$ -lifetime between 40 – 100 ns. It is thus possible that low energetic electrons even

in the afterglow can excite the $N_2(A)$ to the $N_2(B)$ state and contribute to the FPS emission.

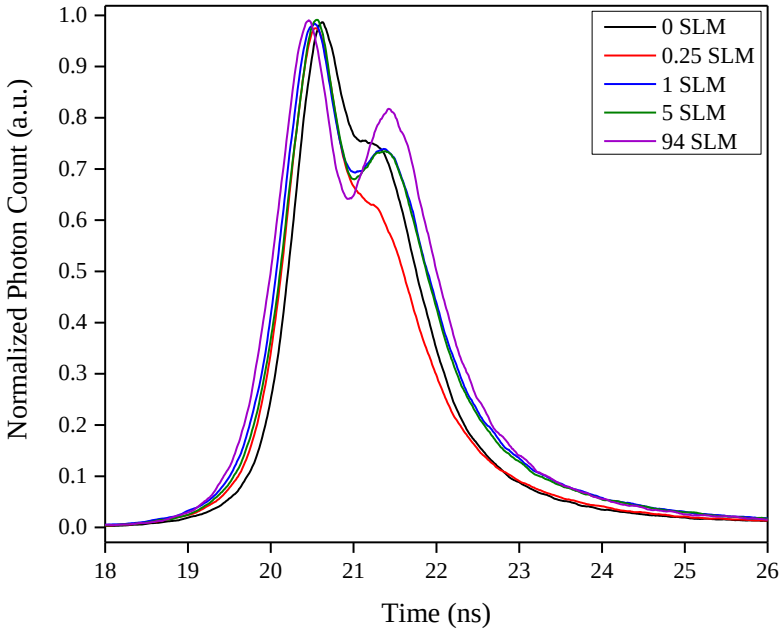

Figure 1.8. Normalized temporal evolution of $N_2^+(B\ ^2\Sigma_u^+ \rightarrow X\ ^2\Sigma_g^+)$ (0, 0) at 391.5 nm (FNS) as a function of air flow rate.

The NO-γ emission is initially time aligned with the discharge event but has a long tail. The maximum intensity of the NO-γ emission drops by only a factor 1.3 while the tail is significantly reduced for the 94 slm case compared to the 0 slm case. The production of NO(*A*) studied in detail in [25] suggests the production of NO(*A*) by $N_2(A)$ in the afterglow with an excitation rate of 5.5×10^{-11} cm^3s^{-1} [24].

$$N_2\left(A^3\Sigma_u^+\right) + NO\left(X^2\Pi\right) \rightarrow N_2\left(X^1\Sigma_g\right) + NO\left(A^2\Sigma^+\right) \quad (1.3)$$

This reaction can explain the tail of the NO-γ emission. The flow could thus impact the NO(*A*) emission intensity through the depletion of the NO ground state and the $N_2(A)$ density. However the lifetime of $N_2(A)$ is significantly lower than the gas residence time which suggests that the main impact of the gas flow is the reduction in the NO(*X*)

density. As the NO production occurs in the afterglow and not during the active microdischarge lifetime emission [26], this will impact both the peak intensity as well as the tail.

Figure 1.9 shows that indeed adding NO to the discharge impacts both the peak intensity and tail of the NO(*A*) emission, very similar to the flow effect suggesting that the NO(*A*) intensity correlates with the NO(*X*) density.

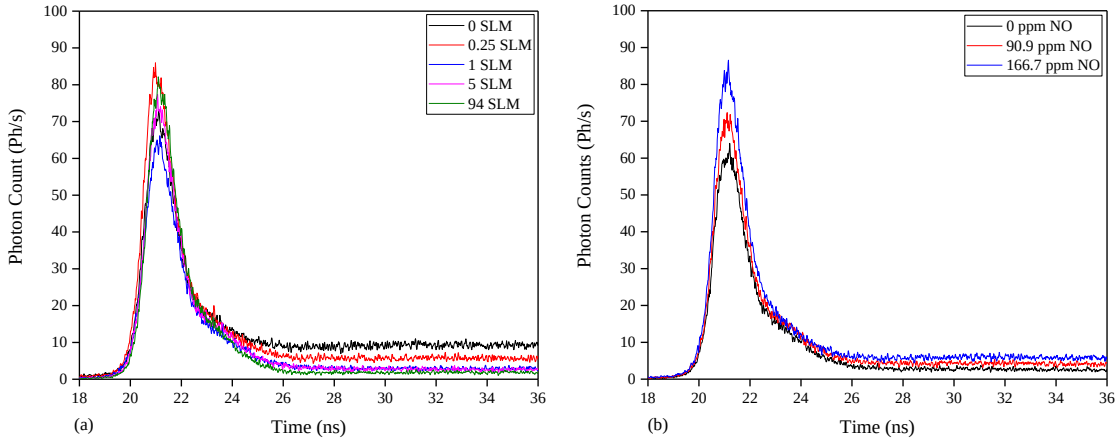

Figure 1.9. Temporal evolution of NO($A\ ^2\Sigma^+ \rightarrow X\ ^2\Pi$) (0, 0) emission at (a) various air flow rates, and (b) various concentrations of NO added to 5 SLM air flow rate at 5.7W.

1.3.4. Electric field strength as function of flow rate

The electric field strength is determined using the procedure described in *Section 1.2.5*, and plotted in Figure 1.10 as a function of flow rate for the positive and negative half cycle. A temperature difference of 50 K exists between 0 and 94 slm. The corresponding density differences are taken in consideration to calculate the effective lifetime of the $N_2(C)$ and $N_2^+(B)$ states. The maximum reduced electric field at the location of maximum intensity is estimated to be 714 Td during the positive half cycle, while the E/N values are smaller in the negative half cycle.

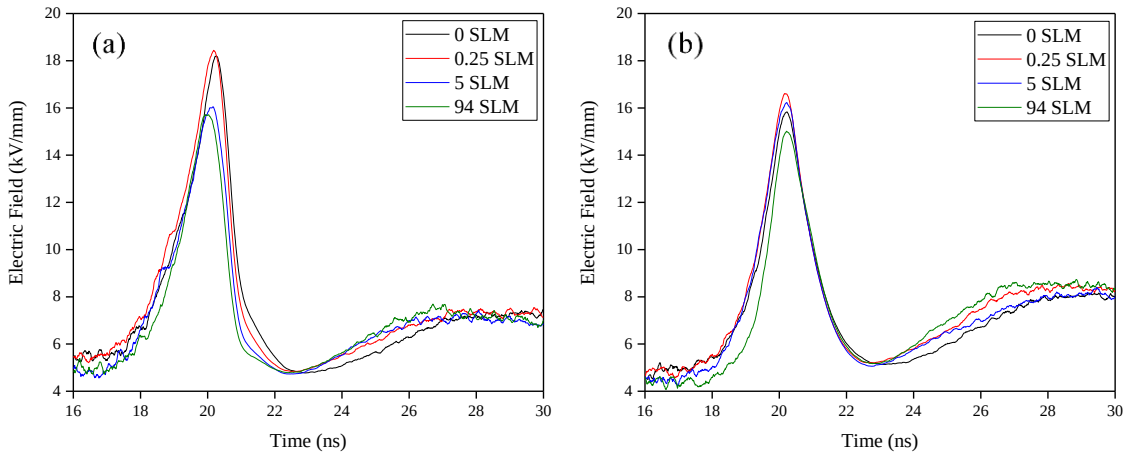

Figure 1.10. Temporal electric-field strength evolution obtained from the ratio of SPS and FNS transitions as a function of flow rate. The discharge power is kept constant at 5.7 W. (a) Positive half cycle and (b) negative half cycle.

The general trend suggests that the field is reduced with higher flow rates, except for no flow condition in the negative half cycle. The difference in the electric field strength at no flow condition and 94 slm is 13.7%, which is similar to the 14.8% increase in the neutral density. The pressure difference of 3000 Pa in the hole due to the flow plays an insignificant role in the change in density. E/N, the reduced electric field strength is dependent on the flow rate. The rise of the electric field in the positive half cycle occurs at the same time, while the decay is faster for higher flow rates. In the negative half of the cycle, a delayed rise for higher flow rates but identical decay of the electric field is observed. Also a local dip in the electric field evolution is evident after which a second maximum starts to appear at 23 ns. Similar observation has also been reported in [27]. Since this electric field is determined from a line integrated measurement, the increase and decrease in the electric field does not necessarily reflect a variation in the electric field on a single location. After the propagation phase, the electric field in the filament starts to reduce. This reduction in electric field coincides with a reduction in the emission

intensity but an increased emission intensity has been observed for surface discharges after the main discharge event [27]. Although there is not a formation of cathode layer, this secondary rise in the field might be initiated by the formation of a space-charge. The estimated amplitude of the reduced electric field in the gap (0.5 mm) with an applied voltage amplitude of 10.8 kV is 10.8 kV/mm, which is of the same order as found through the 2D stationary electrostatic simulation of the microdischarge source (7.5 – 12.5 kV/mm) as shown in Figure 1.11. The bended field lines are also consistent with a plasma streamer or filament that is detached from the dielectric surface.

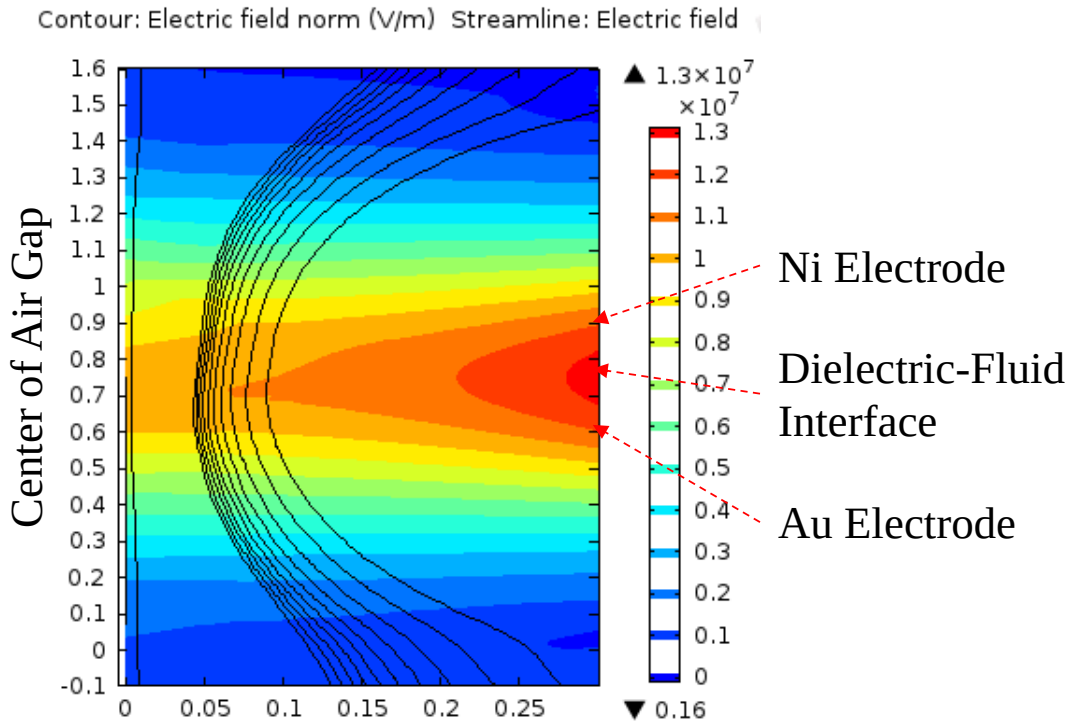

Figure 1.11. Electric field simulation in the air gap using COMSOL Multiphysics 5.0 stationary electrostatics domain.

1.3.5. Spatially resolved electric field distributions

Additionally, the spatially-resolved evolution of the electric field strength is shown for the positive and negative half cycles in Figure 1.12 for the case of 0 and 94 slm. In the

figure, the location of maximum intensity is defined as 0 μm, with 75 μm near the surface of the hole and -75 μm, away from it. At higher flow rate, not much difference is noted. The field strength is highest at the location of maximum intensity with a faster rise time of 1.5 ns, and becomes smaller close to the hole-surface. However, at no flow condition, the field strength decreases gradually away from the hole-surface. Higher flow rate should enhance the removal of ionized and metastable species, which requires higher fields to generate plasma. $N_2(A)$ is not expected to play a role in the breakdown as the lifetime of $N_2(A)$ is much lower than the discharge period.

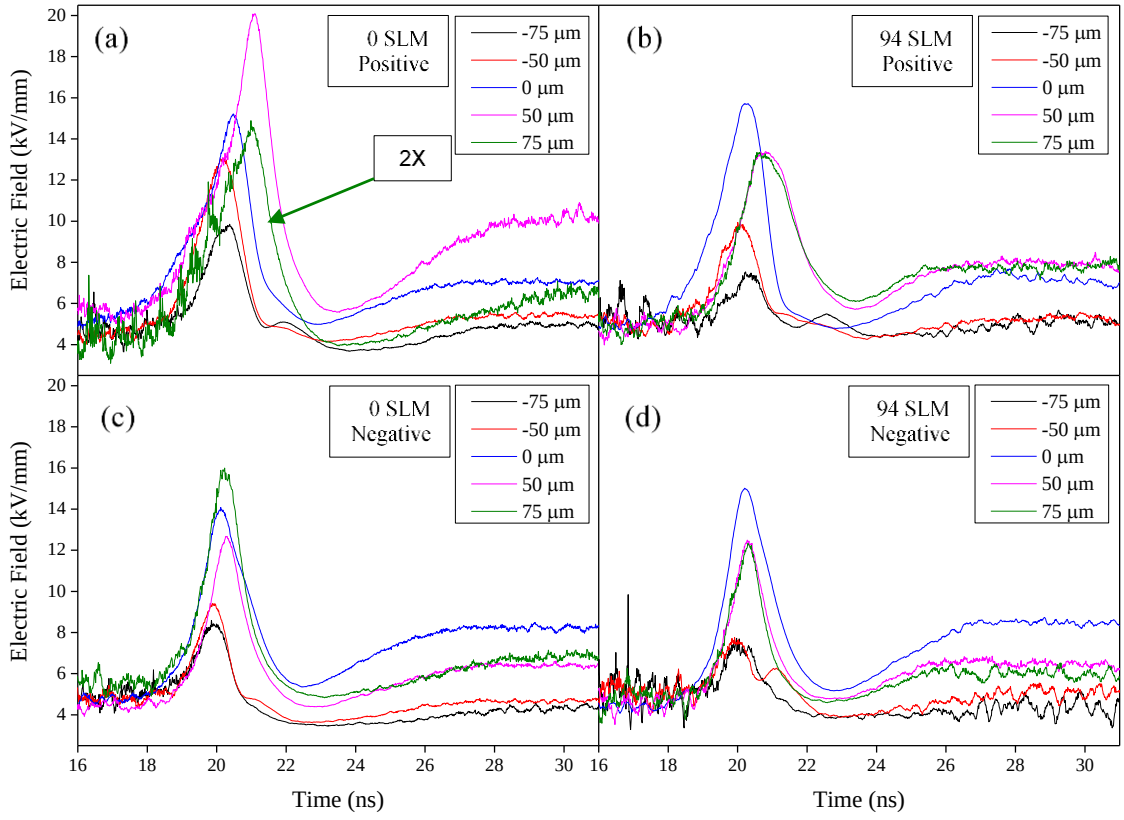

Figure 1.12. Spatio-temporal electric-field strength evolution obtained from the ratio of SPS and FNS transitions. The discharge power is kept constant at 5.7 W. (a) 0 SLM, positive half cycle, (b) 94 SLM, positive half cycle, (c) 0 SLM, negative half cycle, and (d) 94 SLM, negative half cycle. Note that the electric-field strength of one of the curves in (a) is reduced by a factor of 2.

The $N(^4S)$ and $N(^2P)$ state can have a lifetime of the order of a few ms [26]. However their densities will be significantly lower than the densities in nanosecond repetitive pulsed spark discharges as investigated by Laux [28] and Popov [29]. Hence they are not expected to play a major role in the ignition of this dielectric barrier discharge.

The convective flow will most likely reduce the main long-lived species produced by the DBD such as O_3, NO, N_2O, NO_3, N_2O_5 and NO_2. All of these species are electronegative, but their absolute electron attachment cross-sections are of the same order as that of O_2 and the maxima in these cross-section are at similar or smaller values than that for O_2. The only exceptions are NO having maximum cross section at 8.15 eV and O_3 with cross-section up to 21.5 times larger at 1.4 eV than O_2 [30–32]. These species are present at a value of at most 500 ppm, which is at least 400 times less than O_2. It is thus unlikely that the electron attachment to these species will affect the discharge generation, particularly as the E/N is in excess of 200 Td in this case. Electron attachment becomes larger than ionization for reduced electric fields equal to or less than 120 Td at atmospheric pressure [40].

The variation in the electric field distribution can only be explained by differences in the space-charge distribution, which can be reduced by high gas flow [11].

The air at 94 slm is with 0% RH, while the room air contained 35% RH (1% water). Hence it is imperative to discuss the impact of humidity on the electric field. Water impurities at these concentrations are not expected to impact the attachment [33]. Humidity affects however the mobility of the ions, which might give rise to different space-charge distribution in dry and humid air.

With increasing humidity, both the positive and negative ion mobility reduces. The mobility of positive ions equal about 2.2×10^3 cm^2/Vs and 0.61×10^3 cm^2/Vs for dry and humid air, respectively at 293 K and 1 Torr [34]. This indicates that the ions move around 3.5 times faster in dry air than in humid air. For 35% RH and 1 atm, the mobility values are 1.4 cm^2/Vs and 1.8 cm^2/Vs for positive and negative ions, respectively [35].

High flow rates seem also to give rise to a second maximum in the electric field, which could be due to an ionization event at another location in the micro-discharge hole but could also correlate to a discharge event from neighboring holes due to the cross-correlation process. A detailed investigation of the effect of humidity on the electric field distribution should preferentially be performed in a discharge geometry that allows a spatially resolved measurement of the electric field without the complication of the analysis of the line integrated averaged data obtained for the investigated discharge in this work.

1.4. Conclusion

A two-dimensional array of microdischarges is generated in air at atmospheric pressure and at different flow rates with the highest flow rate having a gas residence time approximately equal to the discharge period. A comparison of the voltage and current waveforms for different flow rates, shows that the discharge is significantly affected by the gas flow. A unique voltage-charge plot is obtained with elongated dark periods (no discharge activity) and inhibition effect of additional microdischarges due to the surface charge accumulation. The gas temperature is determined by determination of the rotational temperature obtained from the molecular band of (0,0) transition of the second

positive system of N_2 at 337.1 nm. The gas temperature does not exceed 350 K. A very significant effect of flow on NO emissions is observed, and for increasing residence time, the NO density becomes larger. Using the emission intensities of SPS and FNS, reduced electric fields are obtained with a maximum equal to 714 Td and 641 Td at 0 slm and 94 slm, respectively in the positive half of the cycle, significantly dependent on the gas flow. Finally, it is suggested that the space-charge distribution changes with the flow rate play a major role in the evolution of electric field in this configuration. Both flow rate and a reduction in water impurity changing the ion mobility can be responsible for the observed effect.

Chapter 2: Ozone and Singlet Delta Oxygen production [2]

2.1. Introduction

Singlet delta oxygen, $O_2(a\ ^1\Delta_g)$ is the first electronically excited state of molecular oxygen, having an excitation energy of 0.98 eV [36]. Over the last decade, it has been recognized as a specie playing a major role in atmospheric plasma chemistry, biology, medicine and plasma-assisted combustion [37]. Because of its low excitation energy, it has a relatively long lifetime and can reach significant densities.

The well-known photodynamic therapy (PDT) for cancer treatment uses photosensitizers irradiated with visible to near-IR light to selectively kill the cancerous cells. PDT produces $O_2(a\ ^1\Delta_g)$, which is the primary cytotoxic agent and responsible for the inactivation of cancer cells [38]. Plasmas can also be efficient sources of $O_2(a\ ^1\Delta_g)$ and are studied in the context of cancer treatment [37]. Recently the Food and Drug Administration (FDA) approved the use of PDT for treatment of esophageal and certain lung cancers [39]. In this context, it is of utmost importance to gather more data on $O_2(a\ ^1\Delta_g)$ production in various discharge systems and their biological impact. Aboubakr *et al* [40] recently showed for example that plasma-produced $O_2(a\ ^1\Delta_g)$ is effective in inactivating feline calicivirus.

Apart from biological applications, many studies have been performed on the effect of $O_2(a\ ^1\Delta_g)$ on plasma-assisted combustion. It has been shown that the oxidation of methane in air can be accelerated by the effective use of the energy of electronic

[2] This chapter described work that is collaboratively performed with Dr. João Santos Sousa from Laboratoire de Physique des Gaz et des Plasmas (LPGP), Paris, France. The calibrated SDO measurement cell has been provided by Dr. Sousa and measurements are performed jointly with Dr. Sousa.

excitation in the presence of $O_2(a\ ^1\Delta_g)$ at low gas temperatures [41]. Indeed, it is capable of increasing the rate constant of a chemical reaction by reducing its activation barrier [36]. Smirnov *et al* showed that even a small concentration of $O_2(a\ ^1\Delta_g)$ (~1%) in the H_2-O_2 mixtures can reduce the period of the ignition delay significantly and ignite the gas mixture at lower gas temperatures [42]. Additionally, the kinetics of the reactions of C_2H_4 with $O_2(a\ ^1\Delta_g)$ have been studied to understand the plasma-flame kinetics and propagation mechanisms at low pressure [43]. The presence of $O_2(a\ ^1\Delta_g)$ enhances the speed of flame propagation in C_2H_4.

Modeling work has been performed previously to estimate $O_2(a\ ^1\Delta_g)$ density in a nanosecond pulsed air discharge at pressures ranging from 40-100 Torr [44]. A 0D numerical simulation of the chemical kinetics in a dielectric barrier discharges in the context of ozone formation in air is reported which includes an estimate of the $O_2(a\ ^1\Delta_g)$ density evolution [26].

$O_2(a\ ^1\Delta_g)$ is produced by electron-impact excitation from the ground state density

$$e^- + O_2 \rightarrow O_2\left(a^1\Delta_g\right) + e^- \tag{2.1}$$

while the major loss mechanisms are collisional quenching:

$$O_2(a^1\Delta_g) + O_2 / N_2 / O_3 \rightarrow O_2 + O_2 / N_2 / O_3 \tag{2.2}$$

Sousa *et al* reported $O_2(a\ ^1\Delta_g)$ densities of 10^{22} m^{-3} in atmospheric pressure Micro-Cathode Sustained Discharge generated in $He/O_2/NO$ mixtures [45]. Small concentrations of NO have been introduced in He/O_2 mixtures to quench O_3, a major quencher of $O_2(a$

$^1\Delta_g$)and increase the $O_2(a\ ^1\Delta_g)$ density [45]. In this work, we will investigate the $O_2(a\ ^1\Delta_g)$ generation in a dielectric barrier discharge in air.

Many applications that rely on $O_2(a\ ^1\Delta_g)$ require sensitive diagnostics technique to measure, monitor and control the production of $O_2(a\ ^1\Delta_g)$ in order to optimize the relevant processes. Some of the notable optical diagnostics include absolute emission spectroscopy, intracavity laser absorption spectroscopy, off-axis integrated cavity output spectroscopy (ICOS) and radar resonance-enhanced multiphoton ionization (REMPI) [46]. Radar REMPI allows for highly sensitive non-obtrusive $O_2(a\ ^1\Delta_g)$ density measurements with high spatial resolution and sensitivity. However, it requires highly complex and expensive equipment.

The presented work in this paper is the first attempt of its kind to experimentally determine the $O_2(a\ ^1\Delta_g)$ absolute density in an atmospheric pressure DBD in air consisting of a two dimensional array of micro-discharges using IR optical emission spectroscopy. As ozone is one of the main quenchers of $O_2(a\ ^1\Delta_g)$, the ozone density has also been measured at the same discharge conditions.

The structure of this chapter is as follows. First we present the discharge, singlet delta oxygen and O_3 measurement techniques. The results are discussed in *Section 2.3*, before we present our conclusions.

2.2. Experimental Setup and Methods

2.2.1. Plasma Discharge

The two dimensional array of micro-discharges is operated in ambient air at different flow rates ranging from 16.4 slm to 94 slm and at varying discharge power. The

discharge power is measured using the voltage-charge integral method (Lissajous figure) as described in Chapter 1. The highest increase in gas temperature will be for the condition 28.3 slm and 10.5 W. The maximum increase in temperature can be estimated from a thermal balance assuming that all heat is removed through forced convection by the gas flow:

$$\Delta T = \frac{P}{\dot{m} C_p \rho} \approx 18K \tag{2.3}$$

with P the discharge power, $\dot{m}$ the mass flow rate, C_p the specific heat at constant pressure and ρ the density of air. The effect of gas heating can be neglected in this study.

2.2.2. Ozone density measurement

The ozone (O_3) density in the gas phase is determined using ultraviolet (UV) absorption spectroscopy [45]. Figure 2.1 shows the schematic of the setup used for the ozone measurements. A mercury-neon lamp is used as a UV light source at one end of the cell, and more specifically the 254 nm mercury emission line. The effluent from the discharge is allowed to pass through an absorption cell with an effective path length of 82 mm. This absorption cell is coupled to the base of the micro-discharge reactor through a chalice-shaped glass mounting. A neutral density filter is placed between the lamp and the absorption cell to reduce the intensity of the mercury lamp. The light is collected through a lens attached to an optical fiber connected to a low resolution spectrometer (Avantes AvaSpec-2048). The transmitted light intensities are recorded as a function of time when the plasma is on and off. The light intensity is integrated between 253 and 255 nm for more accurate O_3 density measurements as described in [45]. By comparing the ratio of

the temporal evolution of the intensities transmitted when the plasma is on (I) and off (I_0) alternatively, the absolute O_3 density can be obtained by the Beer-Lambert law:

$$-\ln\left(\frac{I}{I_0}\right) = \sigma N l \tag{2.4}$$

where N is the absolute ozone density, σ is the absorption cross section of ozone (1147×10^{-24} m^2) at 254 nm [47] and l is the absorption length (82 mm) [45]. The spatial distribution of ozone in the absorption cell is assumed to be homogeneous. This is a valid assumption because all the gas is flowing through the discharge area and O_3 has a lifetime significantly longer than the residence time in the absorption cell (see also further).

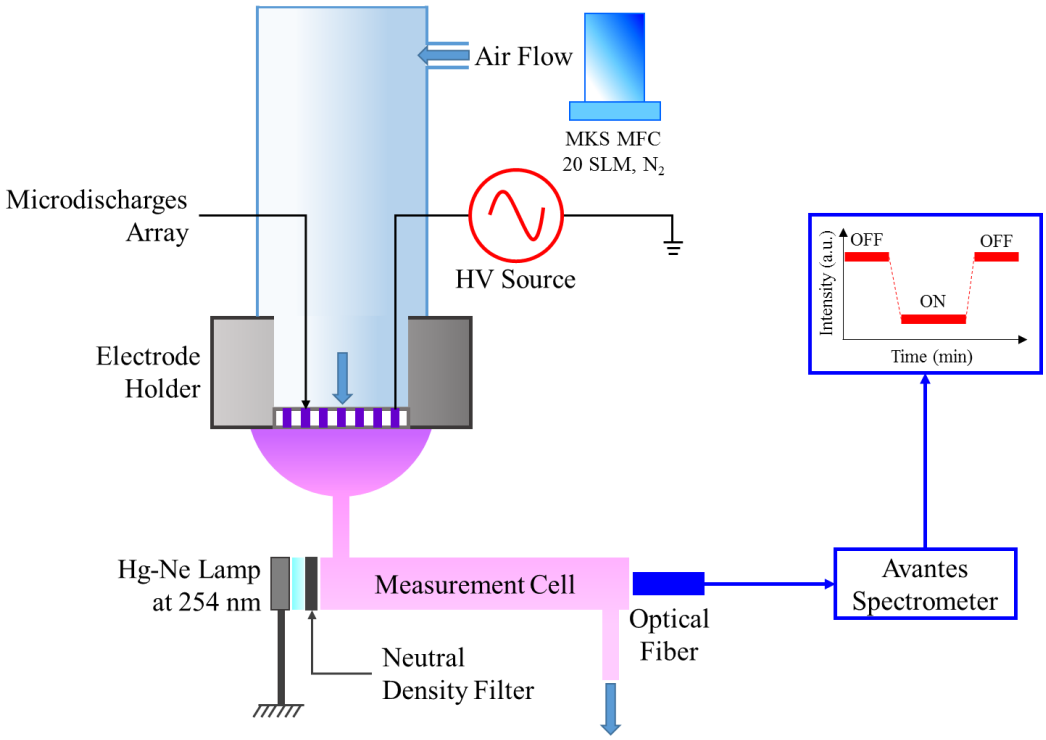

Figure 2.1. Schematic of the ozone density measurement using UV absorption spectroscopy.

2.2.3. Absolute singlet delta oxygen (SDO) density measurement using IR OES

Infrared (IR) radiation at a wavelength of 1.27 μm is emitted during the radiative decay of $O_2(a\ ^1\Delta_g)$ to $O_2(X\ ^3\Sigma_g^-)$. The Einstein coefficient for this transition is $A = 2.22\times10^{-4}\ s^{-1}$, resulting in a radiative lifetime of 75 minutes [36]. The absolute emission intensity relates to the density of $O_2(a\ ^1\Delta_g)$, however, the emission signal is extremely weak and needs a sensitive detector to enable its measurement. The measurement technique is identical to the methods used in Sousa *et al* [45], and the experimental setup is shown in Figure 2.2. The setup consists of a SDO measurement cylindrical cell (82 mm long) with two quartz windows to allow detection of the emission (11 mm effective diameter). The cell is coupled to the DBD reactor using a chalice-shaped, sealed glass mounting. An InGaAs detection system is used to detect the emission signal, which is coupled to an IR filter (Andover 200FC39-25/1270) centered at 1.27 μm. In order to distinguish the signal from the background noise, an operational amplifier is used (10^7 gain). The detectors used are identical to the ones presented in [45]. An oscilloscope (Tektronix DPO2024B, 200 MHz bandwidth) is used to monitor the detector's amplified signals and acquire large number of time-averaged data to reduce the noise, for the conditions when the plasma is on and when it is off (background noise).

The amplitude of the detected signal can be converted to corresponding SDO absolute density by utilizing the following optical parameters – sensitivity of the InGaAs detector ($0.9\ AW^{-1}$), transmission of IR filter (35% at 1.27 μm), the geometrical dimensions of the optical detection system and the Einstein coefficient for this transition, *A*. The measurement cell has previously been calibrated using a Monte Carlo simulation which

determines the probability of a photon emitted in the cell reaching the detector (1.9×10^{-4}) [48]. This resulted into a conversion factor of 3.77×10^{15} $O_2(a\ ^1\Delta_g)$ cm^{-3}/mV [45]. The technique has also been previously validated with VUV absorption [45]. Signals with amplitude as low as 10 μV can be detected by the setup. This corresponds to an $O_2(a\ ^1\Delta_g)$ density of 4×10^{13} cm^{-3}.

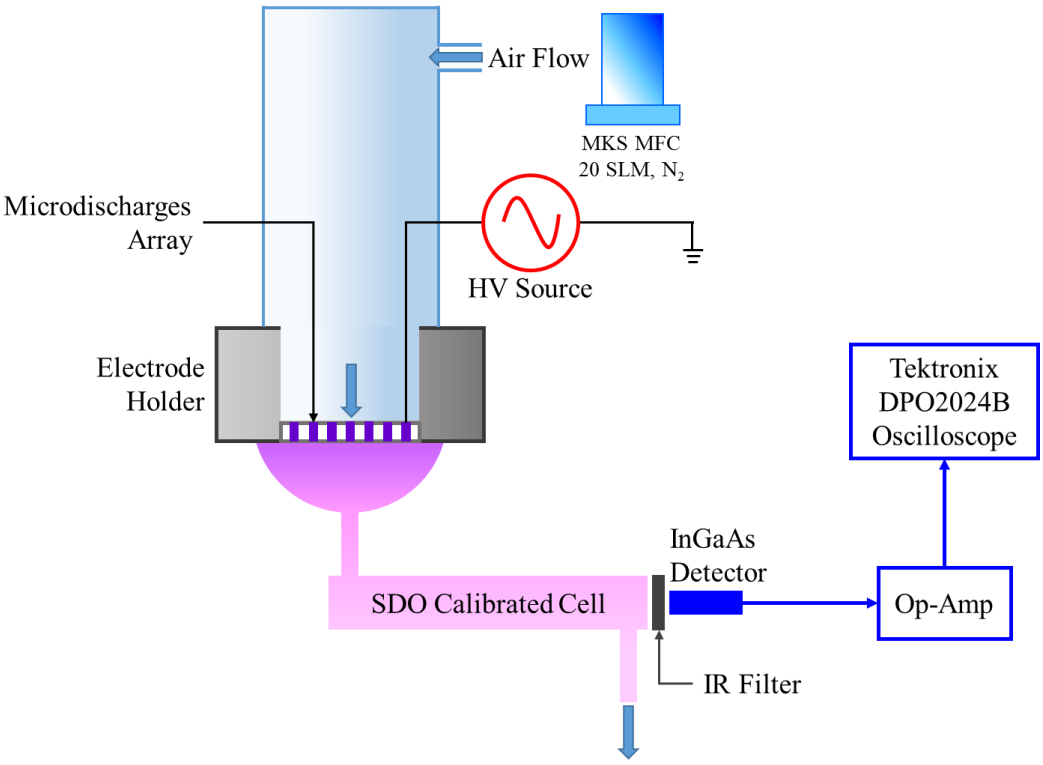

Figure 2.2. Schematic of the experimental setup used for the measurement of the absolute density of singlet delta oxygen [$O_2(a\ ^1\Delta_g)$] by IR optical emission spectroscopy.

2.3. Results and Discussions

2.3.1. Effect of flow rate

The absolute density of $O_2(a\ ^1\Delta_g)$ is measured as a function of air flow rates and discharge power in the afterglow of the DBD. Figure 2.3 shows the O_3 and $O_2(a\ ^1\Delta_g)$ density as a function of air flow rate at a constant discharge power of 5.6 ± 0.1W. The

absolute O_3 density reduces gradually with flow and varies from 5.1×10^{21} m^{-3} at 20 slm to 1.1×10^{21} m^{-3} at 94 slm. The measured $O_2(a\ ^1\Delta_g)$ density in the absorption cell increases with flow rate and saturates for higher flow rates. The actual $O_2(a\ ^1\Delta_g)$ density as produced by the plasma can be determined by using the gas residence time t_{res} and the lifetime τ of the $O_2(a\ ^1\Delta_g)$ in the afterglow. The gas residence time, t_{res} in the afterglow is determined as a function of flow rates, considering the effective combined volume of the SDO measurement cell and the coupler equal to 3.5×10^{-5} m^3. The $O_2(a\ ^1\Delta_g)$ density in the measurement cell can be written as –

$$\frac{dn_{SDO}}{dt} = -\left(k_{N_2} n_{N_2} + k_{O_2} n_{O_2} + k_{O_3} n_{O_3} + \frac{1}{\tau_{rad}} \right) n_{SDO} = -\frac{n_{SDO}}{\tau} \tag{2.5}$$

$$\frac{n_{SDO}(t_{res})}{n_{SDO}(t=0)} = \exp\left(-\frac{t_{res}}{\tau} \right) \tag{2.6}$$

where $n_{SDO}(t_{res})$ is the measured $O_2(a\ ^1\Delta_g)$ density in the afterglow, $n_{SDO}(t=0)$ is the $O_2(a\ ^1\Delta_g)$ density as produced in the discharge, τ_{rad} is the radiative lifetime of $O_2(a\ ^1\Delta_g)$ which can be neglected and τ is the effective lifetime of $O_2(a\ ^1\Delta_g)$ in air at atmospheric pressure and room temperature. In the above equation, the quenching of O_3 is included although the quenching effect of NO and NO_2, which is much less efficient than O_3, is neglected [49]. The effective lifetime of $O_2(a\ ^1\Delta_g)$, $\tau_{eff}^{O_2(a)}$ becomes equal to the residence time, $t_{res\ cell}$ at a flow rate of 21.6 slm (without considering quenching by O_3). It is thus of the utmost importance to correct the measured singlet oxygen densities in the effluent to obtain densities as produced by the discharge.

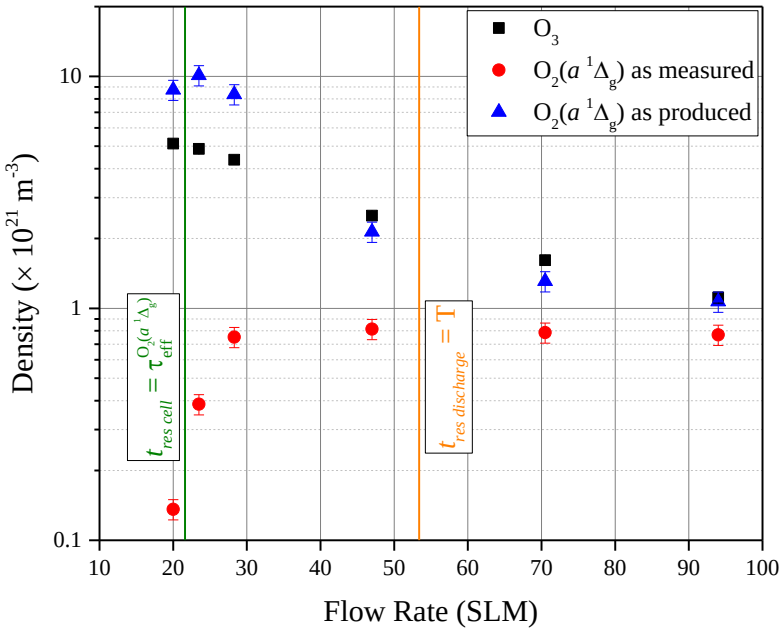

Figure 2.3. O_3 and $O_2(a\ ^1\Delta_g)$ absolute density with flow rates at a constant discharge power of 5.6 W. The flow rates for which the residence time equals one discharge cycle and the lifetime of $O_2(a\ ^1\Delta_g)$ in air is also indicated.

The densities in Figure 2.3 can be attributed to different flow effects. At higher flow rates (47 to 94 slm), the estimated $O_2(a\ ^1\Delta_g)$ density in the discharge has the same trend as the O_3 density. The gas residence time in the discharge, $t_{res\ discharge}$ becomes equal to the time period of one voltage cycle, T at a flow rate of 53.4 slm, which means that for flow rates in excess of 53.4 slm, every new discharge happens after O_3 and $O_2(a\ ^1\Delta_g)$ from previous cycle are removed from the discharge zone.

The energy available per air molecule decreases for increasing flow rate. To assess this effect, Figure 2.5 shows the production rates of O_3 and $O_2(a\ ^1\Delta_g)$ (molecules/s) at constant power of 5.6W as a function of the volume specific energy which is determined by the ratio of the discharge power to the flow rate (eV/molecule of air treated). The rate of O_3 production is in first approximation independent of the specific energy, while the $O_2(a\ ^1\Delta_g)$ production rate is larger when $t_{res\ discharge}$ becomes larger than one AC period.

This suggests that the $O_2(a\ ^1\Delta_g)$ density accumulates over multiple discharge events. At low discharge power of 5.6W, around 1.4 μJ is dissipated from each hole during half a period. Using 30% of the volume of each hole (corresponding to the emission zone), the specific energy density is estimated to be 10.5 mJ/cm^3, which is similar to the conditions adopted by Eliasson and Kogelschatz to model the species densities in a micro-discharge in air [26] and shown in Figure 2.4.

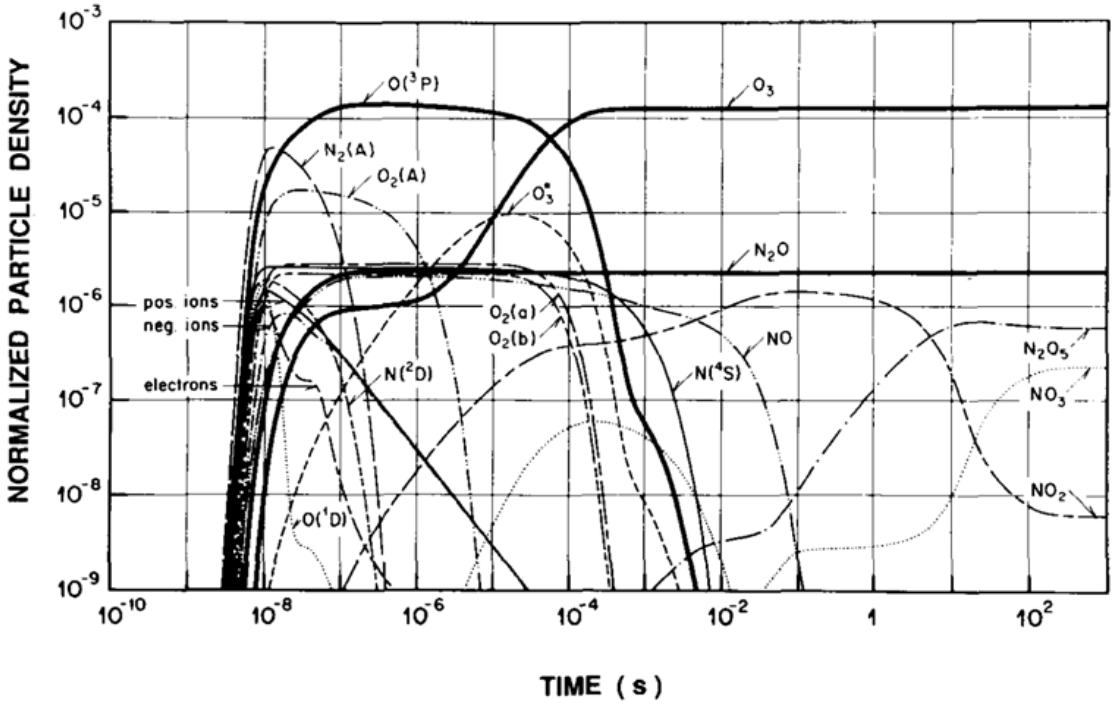

Figure 2.4. Time dependent species density obtained from a 0-D chemical kinetics model for conditions relevant for a micro-discharge in atmospheric pressure air [14].

Comparison between the timescale of O_3 production (20 μs) [47, 26] and the gas residence time in the discharge zone implies that large part of O_3 is formed outside the discharge region ~20 microseconds at 94 slm. The timescale for $O_2(a\ ^1\Delta_g)$ production is similar to the time duration of a single micro-discharge event (~tens of nanoseconds). Hence all $O_2(a\ ^1\Delta_g)$ is produced within the discharge zone. At a low flow rate of 21.6

slm, $t_{res\ discharge}$ becomes 2.5 times T, which suggests accumulation of $O_2(a\ ^1\Delta_g)$ from more than 2 previous voltage cycles, possibly increasing the $O_2(a\ ^1\Delta_g)$ density. Indeed the $O_2(a\ ^1\Delta_g)$ density as produced for 20 slm is two times the density at flow rates of 94 slm . This suggests that quenching of $O_2(a\ ^1\Delta_g)$ in the discharge volume is minimal. The small reduction with increasing specific energy (Figure 2.4) could be due to the quenching of ozone by O atoms [47].

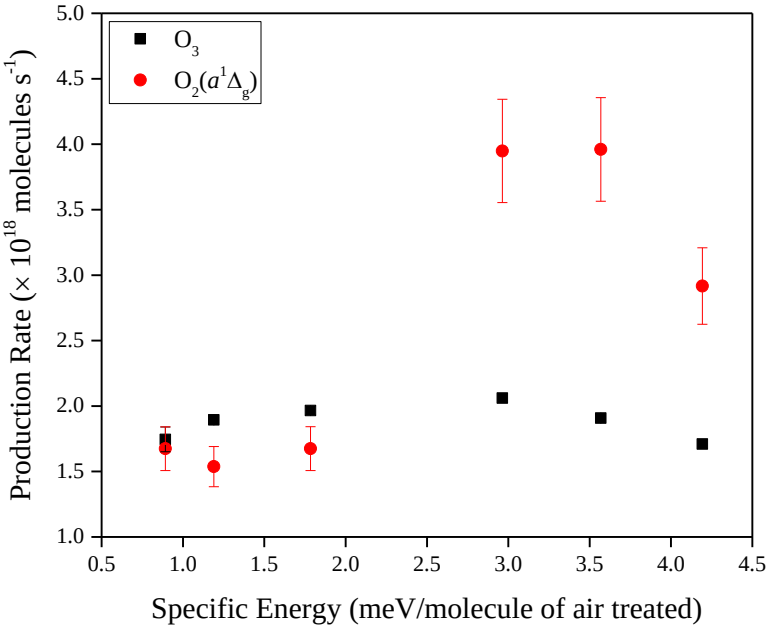

Figure 2.5. Production rate of O_3 and $O_2(a\ ^1\Delta_g)$ at 5.6W but variable air flow rates as a function of specific energy.

2.3.2. Effect of discharge power

The O_3 and $O_2(a\ ^1\Delta_g)$ densities as a function of discharge power for 20, 28.3 and 94 slm are shown in Figure 2.6. Different dependencies of $O_2(a\ ^1\Delta_g)$ density on power for different flow rates are observed. Increasing and decreasing densities of $O_2(a\ ^1\Delta_g)$ have been found related to the presence of NO by Sousa *et al* [45]. At 94 slm, the $O_2(a\ ^1\Delta_g)$ density increases with power showing similar trend as O_3. The O_3 density approximately

increases linearly with power and a similar increase in $O_2(a\ ^1\Delta_g)$ density is observed. The observed effect is similar to the effect of increasing specific energy as observed for varying flow rates. However, at 20 slm, the $O_2(a\ ^1\Delta_g)$ density reduces with power and could not be detected for plasma powers in excess of 6 W. The as produced $O_2(a\ ^1\Delta_g)$ density is still very high as the measured density in the effluent is significantly reduced by the large residence time. More NO is also produced with increasing power and the NO density at 20 slm will be larger compared to 94 slm similarly to the observed O_3 density difference. The ratio of O_3 densities at high and low power is approximately 2 at 94 slm and less than 1 at 20 slm. This suggests an increase in quenching potentially due to a higher O-atom densities at higher specific energies. Figure 2.4 shows a significant reduction in the $O_2(a\ ^1\Delta_g)$ density at 100 μs after the discharge event. This is at the same timescale as $t_{res\ discharge}$ (≈ 134 μs) for 20 slm. This suggest that quenching of the $O_2(a\ ^1\Delta_g)$ is possible to occur in the discharge zone. The higher power density of the discharge will also lead to a higher production of O, NO and O_3 that could be the cause of the reduction in the as produced $O_2(a\ ^1\Delta_g)$ density for increasing power.

At a flow rate of 28.3 slm, the $O_2(a\ ^1\Delta_g)$ density remains constant and reduces only for powers in excess of 8 W. Indeed a smaller residence time will require a higher density of quenchers to reduce the as produced $O_2(a\ ^1\Delta_g)$ density. However, when t_{res} becomes too small, the as produced density will reduce due to a reduction in the specific energy. This provides an explanation of the observed trends but a full chemical kinetics model is required to quantitatively explain the results. While the as produced $O_2(a\ ^1\Delta_g)$ density is always very similar to the O_3 density, varying the flow rate, allows to control the ratio of

the $O_2(a\ ^1\Delta_g)$ and O_3 density in the effluent from 0.7 at 94 slm to intrinsically 0 at lower flow rates. An optimal condition for maximum singlet oxygen generation (1.2×10^{22} m^{-3}) is also found from Figure 2.3 that is a balance between discharge power and gas residence time (t_{res} = 134 μs at 5.34 W). For this condition, the effect of the accumulative singlet oxygen density by multiple discharge events is ideally complemented with a minimum in quenching.

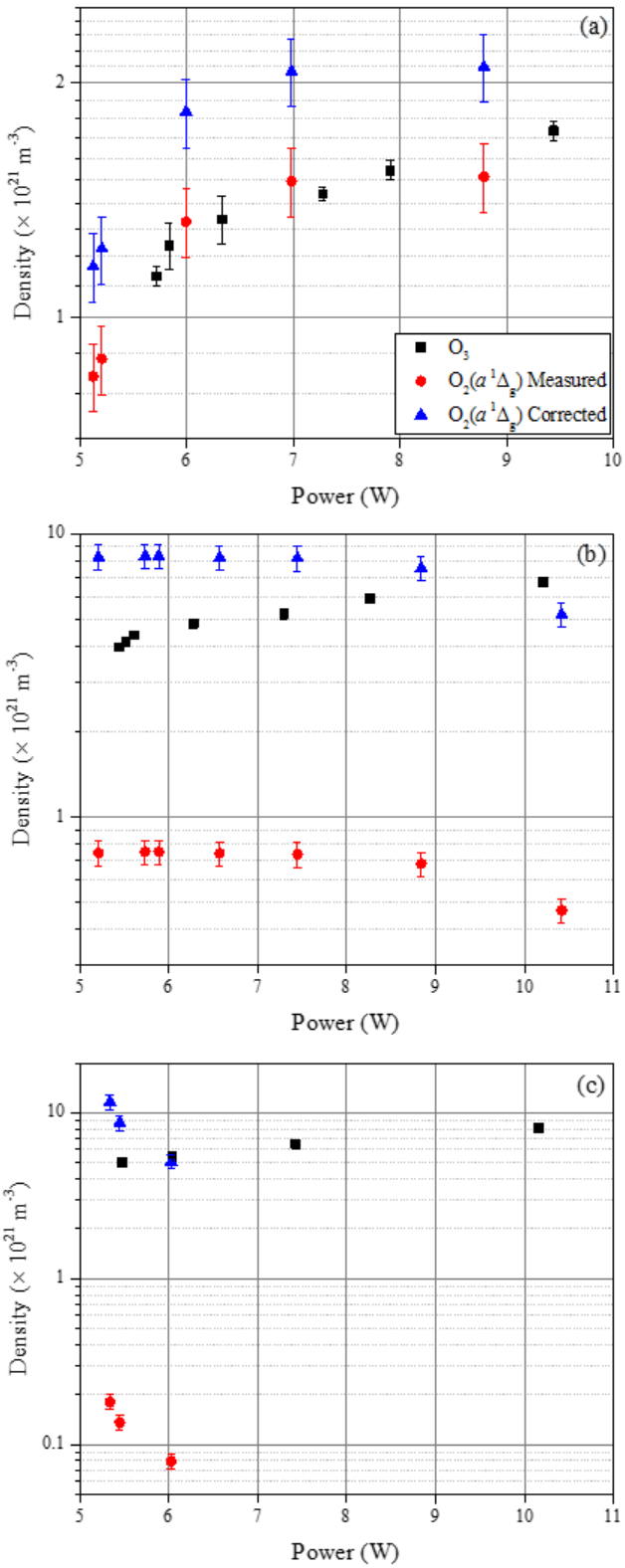

Figure 2.6. O_3 and $O_2(a\ ^1\Delta_g)$ density at varying powers at (a) 94 slm, (b) 28.3 slm and (c) 20 slm.

2.4. Conclusion

The $O_2(a\ ^1\Delta_g)$ density in a DBD consisting of a two dimensional array of micro-discharges in atmospheric pressure dry air is measured for the first time by IR emission. The flow rate (and residence time) and discharge power have a major effect on the $O_2(a\ ^1\Delta_g)$ production and density in the afterglow. The $O_2(a\ ^1\Delta_g)$ as produced by the discharge is obtained from the $O_2(a\ ^1\Delta_g)$ measurements in the effluent by correcting for the collisional quenching and residence time in the measurement cell. The maximum as produced $O_2(a\ ^1\Delta_g)$ density is 10^{22} m^{-3}. The maximum density of $O_2(a\ ^1\Delta_g)$ measured in the effluent for 94 slm is 5×10^{21} m^{-3}. Different $O_2(a\ ^1\Delta_g)$ density dependencies on power have been observed for different flow rates. This can be explained with a variation in the residence time in the discharge region that in principle leads to no quenching at the highest flow rates and increased quenching at low flow rates and higher powers. Finally, the flow rate allows for control of the $O_2(a\ ^1\Delta_g)$ to O_3 density ratio in the effluent from 0.7 to 0!

Chapter 3: Virus inactivation [3]

3.1. Introduction

Disinfection by cold atmospheric pressure plasma (CAP) discharges has recently been widely studied and is one of the fastest emerging fields of plasma medicine [4-5, 50-52]. Because of the low gas temperature and high reactivity CAPs are recognized as effective microbiological disinfecting tools that allow disinfection of heat sensitive substrates. As all CAPs are generated in an open air environment, they produce a highly complex chemistry consisting of reactive oxygen and nitrogen species (RONS). Among the most important reactive species are O_3, $O_2(a\ ^1\Delta_g)$, NO, NO_2, HNO_3, HNO_2, $ONOO^-$, H_2O_2 and OH [6, 53]. The interaction of this complex mixture of reactive species with microbes makes it challenging to unravel the underlying mechanisms of the disinfection process. In addition, the use of large variety of different plasma devices and experimental conditions for these studies result in significant variations in efficacies and underlying mechanisms of the disinfection process for results published by different research groups.

Food-borne bacteria and viruses (such as human Norovirus) particularly in minimally processed or fresh foods have been implicated in many outbreaks of gastroenteritis worldwide and are a real threat to public health. This work has as goal to assess plasma technology as an efficient inactivation method for virus and to investigate the underlying mechanisms. In this work we focus on DBDs generated in air. While there exists a vast

[3] This chapter described work that is collaboratively performed with the group of Professor Sagar Goyal. The biological preparation of the virus and virus titer measurements have been performed by H. Aboubakr. The biological treatments and liquid analysis have been performed jointly.

literature on disinfection by CAP, we only review work in this chapter related to DBDs in air.

The interaction of RONS produced by a surface DBD in air with bacteria has been studied in detail by the group of Graves in a batch reactor [5, 50]. This work shows different modes of operation depending on the plasma power density. Graves *et al* reported that an O_3-dominated low-power mode (<0.2 W/cm^2) is followed by a transition phase leading to a NO_x-dominated high-power mode (>0.25 W/cm^2). The bacterial inactivation in solution is shown to correlate with the aqueous phase ozone concentration. However the inactivation by ozone is only observed to be effective when gas-liquid mixing occurs that enhances the mass transfer of O_3 from the gas to the liquid phase [5]. The inactivation by O_3 is independent of the pH of the treated solution while the work of Lukes showed that when nitrites or peroxynitrite chemistry is involved in the inactivation process, the inactivation of bacteria coincides with a drop in pH [54]. However, similar studies performed by Graves *et al* for surface disinfection of bacteria (without the presence of a liquid) suggests that a high concentration of NO_x is more effective than O_3 [50]. Contrary to these results, Šimek *et al* concludes that for a similar although flow through system both dry and wet air plasma treatment of bacteria on surfaces are dominated by O_3 chemistry, even though a broader range of RONS along with OH and H_2O_2 are suggested to be able to play a role in the observed antibacterial activity [52].

Virus inactivation in solution has also been performed with a similar device as studied by Graves [51]. However it is suggested in this work that O_3 is not the main responsible specie for inactivation but rather reactive nitrogen species. Inactivation of virus by ozone

produced by ozonizers in hospital wards and operating theatres have also been successfully tested [55-56]. In biology, the role of NO as a key mediator in the immune response of the body cells has been investigated in the context of virus inactivation [57]. It is shown that a balance between NO/ROS is a crucial parameter for antiviral activity.

As mentioned earlier, the plasma condition itself might affect the various inactivation pathways. A batch reactor is used for both aqueous and surface treatments in [5, 50], in which accumulation of NO_x and O_3 can lead to reactions between these species and result in different gas phase species densities as opposed to the flow-through reactors used in [51-52]. From a perspective of many applications, a flow-through reactor could prove more efficient and economical than a batch reactor for large scale applications.

We use a flow-through reactor consisting of a two-dimensional array of microdischarges in air to inactivate Feline Calicivirus (FCV), a surrogate for human Norovirus (NV), and compare the results with previous works.

In this chapter, the effects of discharge power, treatment time, exposure distance on virus and acidification of the treated solution are investigated. Section 3.2 describes the experimental setup and methods for virus preparation, gas-phase and aqueous-phase treatments, pH and RONS measurements. The experimental results are shown and discussed in Section 3.3. The conclusions are presented in Section 3.4.

3.2. Experimental Setup and Methods

3.2.1. Plasma setup

In addition to the plasma source described in Chapter 1, a 30 mm × 30 mm PTFE platform fixed on a post is provided directly beneath the source to place the samples as

shown in Figure 3.1. The whole arrangement is placed on a pedestal which can be moved horizontally for ease of retrieval of samples. An enclosure made of an acrylic tube (Φ=45 mm) is provided around the platform to restrict the loss of plasma-produced species due to radial diffusion into the surrounding air. The initial treatments to determine the effect of power, exposure time and distance on the virus inactivation are performed without an enclosure. It is stressed that while the inactivation is enhanced with the enclosure, no changes in the trend of virus inactivation are observed with this added arrangement.

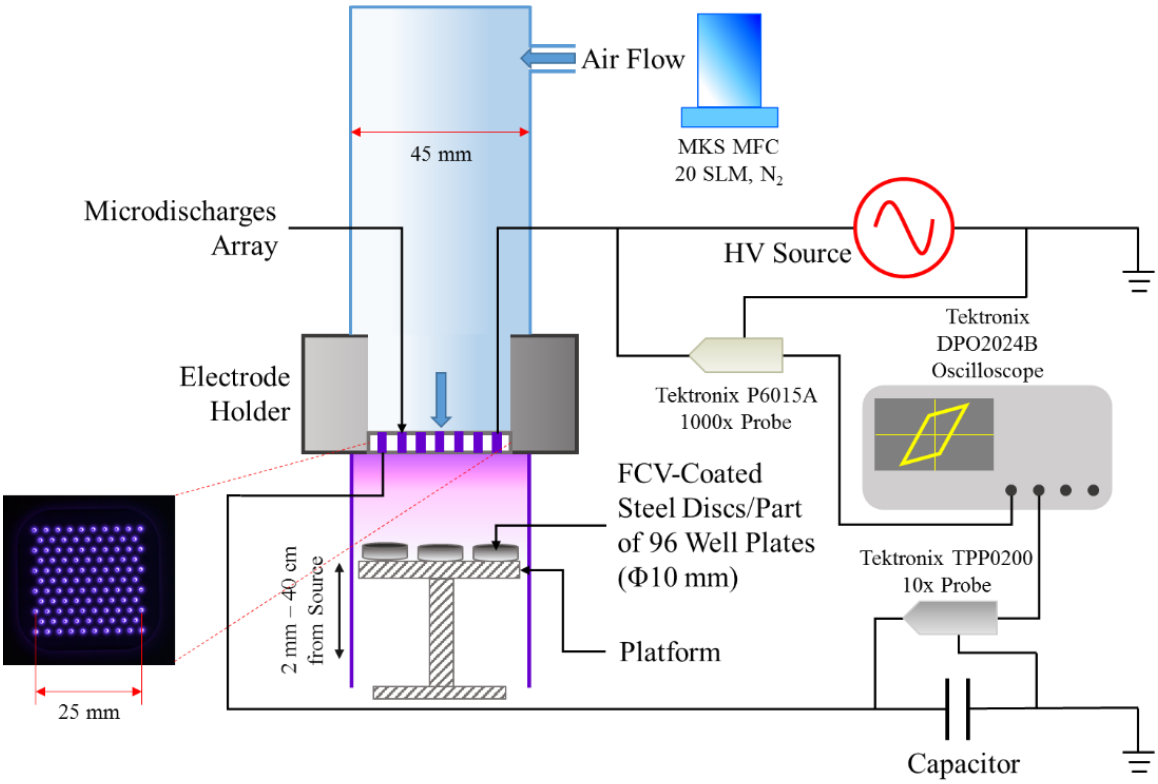

Figure 3.1. Schematic of the experimental setup used for FCV treatment. The platform on which the sample holder is mounted can be linearly displaced between 2mm and 40 cm from the discharge.

The plasma setup can be moved vertically within a range of 2 mm – 40 cm to facilitate various exposure distances for treatment. The flow rate of dry air is controlled at 16.4 slm, unless otherwise stated, by mass flow controller (MKS GE50, MKS Instruments

Inc., USA). The discharge power per cycle, unless otherwise stated, is kept constant at 14.5 ± 0.3 W and is measured using the method described in Chapter 1. The reactive species in the gas phase produced by the microdischarges are blown on the samples, either coated on stainless steel discs or suspended in aqueous medium in a part of 96-well microtiter plates, which are placed on the platform.

3.2.2. Virus assay preparation and titration

The FCV 255 strain is grown and titrated in Crandell-Reese feline kidney (CRFK) cells. The method for growing CRFK cells is described in detail in [9]. The cells containing virus are incubated at 37°C and under 5% CO_2 for 2-3 days after infection, during which period, cytopathic effects (CPE) appear and can be observed under an inverted microscope. The infected cells are frozen and thawed thrice, and then centrifuged and ultra-centrifuged (for further details the reader is referred to [7]) to remove the supernatant. The remaining virus pellet is diluted in 1 ml of sterile distilled water, aliquoted and stored at -80°C until further use.

After the plasma treatment, the steel discs are transferred to sterile dilution tubes containing 1 ml of buffered medium, Phosphate Buffered Solution (PBS) and vortexed for 30 seconds to disperse all virus from the disc into the solution. For virus titration, serial 10-fold dilutions of samples are prepared by adding 20 µl of vortexed sample or 20 µl of treated liquid to 180 µl of minimum essential medium (MEM) containing 4% fetal bovine serum (FBS) in 3 wells per sample. The virus dilutions are inoculated into previously prepared CRFK cell monolayers in 96-well microtiter plates using 3 wells per dilution. The microtiter plate is incubated at 37°C, 5% CO_2 and 85% RH for at least 4

days to allow for the appearance of CPE (observed under an inverted microscope). The highest dilution of virus at which 50% of the inoculated CRFK cell cultures are infected is considered as the end-point, and the Kärber method is used to calculate the virus titer [58]. The virus titer is expressed as logarithmic value of 50% tissue culture infective doses per 100 µl (log_{10} $TCID_{50}$/100 µl of eluent).

3.2.3. FCV treatment

The initial virus titer contains 10^8 – 10^9 plaque forming units (PFU) per ml of distilled water. Prior to experiments, the frozen virus is thawed and diluted to around 10^6 PFU/ml. For surface treatment, stainless steel discs (Φ=10 mm) are sterilized and placed in the wells of 24-well microtiter plate, with the convex surface facing up. 10 µl of diluted FCV sample is spread on the top surface of each disc, and kept to dry for 30 minutes before treatment. For liquid treatment, aliquots (100 µl) of FCV suspended in liquid is prepared by adding 10 µl of FCV to of 96-well plate in triplicates, containing 90 µl of DW or NaCl-Tris-EDTA buffer (NTE) each, as required. All liquid-phase treatments are performed right after the virus has been added to the wells. 3 FCV-coated steel discs or part of 96-well microtiter plate are placed directly beneath the plasma source on the platform at specified treatment conditions (exposure time and distance) and simultaneously treated. For wet treatment, the steel discs are sprayed with a burst of sterile distilled water using a size-adjustable multi-nozzle bottle every 2 minutes starting right before the treatment. A delay of 2 minutes for wetting the surface is chosen because for the highest plasma power condition with maximum temperature rise, it is found that the surface is almost dried up after 2 minutes of treatment. For both dry and wet surface

treatment of FCV, flow controls (subjected to same treatment conditions without the plasma) are considered to account for the scraping of virus coating from the surface of the disc during treatment, in addition to the non-treated controls.

3.2.4. Time-delay measurements

100 µl of sterile DW is added to a part of the 96-well microtiter plate in triplicates, and treated for 5 minutes at two exposure distances of 1 cm and 40 cm. 10 µl of FCV is added to each well at various delay times after treatment. The direct treatment of FCV in distilled water at the same condition is taken as the point of reference. The virus titration procedure is started after 5 minutes of adding the virus to the treated liquid. For treatment at 1 cm exposure distance, a very small loss in volume (<10%) of treated water is observed which is compensated by adding sterile DW to increase the volume to the initial 100 µl.

3.2.5. pH measurements

Aliquots of 100 µl of sterile DW or NTE buffer are added to four wells of 96-well microtiter plate and treated by the plasma at 1 and 40 cm exposure distances for treatment times ranging from 1 to 10 minutes. The pH is measured for each well directly after the treatment using a Thermo Fisher Scientific Orion pH probe (8220BNWP, Waltham, MA, USA). The pH is taken to be as the average of the pH of treated liquid in each well.

3.2.6. O_3 *and* $O_2(a\ ^1\Delta_g)$ *densities*

Both ozone (O_3) and singlet delta oxygen $O_2(a\ ^1\Delta_g)$ densities are measured at plasma operating conditions of 14.5 ± 0.3 W and 16.4 slm. The measurement techniques are described in detail in Chapter 2.

3.2.7. Nitrite and nitrate concentrations

A spectrophotometric method based on the Griess assay is used for nitrite (NO_2^-) and nitrate (NO_3^-) quantification as described by Miranda *et al* [59]. The materials required for the measurement are PBS, Griess assay, sodium pyruvate ($C_3H_3NaO_3$) (100 mM, 100x, Sigma-Aldrich), vanadium (III) chloride (VCl_3) (Sigma-Aldrich), sodium nitrite ($NaNO_2$) (Sigma-Aldrich), sodium nitrate ($NaNO_3$) (99.3% Chem-Impex International Inc.) and hydrochloric acid (HCl). 216 mM PBS (pH 7.4) is prepared by adding 10 g FA buffer to 1 liter of sterile DW. The pH is raised to a value of 7.84 by adding minute amount of 1 M NaOH. The Griess reagent is prepared by mixing equal volumes of components A (*N*-(1-naphthyl)ethylenediamine dihydrochloride, 25 mL of a 0.1% (1 mg/mL) solution) and B (Sulfanilic acid, 25 mL of a 1% (10 mg/mL) solution in 5% phosphoric acid) present in the Griess Reagent Kit (G-7921, Molecular Probes). Enough solution is prepared for the entire treatment purpose. Sodium pyruvate solution is prepared by adding 100 µl of sodium pyruvate to 10 ml of sterile DW. Vanadium (III) chloride is used for reduction of nitrate to nitrite in solution, and is prepared by adding 400 mg of solid VCl_3 to 50 ml of 1 M HCl. For calibration purposes, sodium nitrite solutions with concentrations between 10 – 100 µM are prepared by mixing 10 µl of 0.1 M $NaNO_2$ and 9.9 ml of sterile DW and making standard dilutions. Similarly, sodium nitrate solutions (50 – 500 µM) are prepared by mixing 10 µl of 0.1 M $NaNO_3$ and 9.99 ml sterile DW, and making standard dilutions. The calibration plot for both nitrite and nitrate is shown in Figure 3.2. Aliquots (100 µl) of sterile DW are plasma-treated at two exposure distances (1 cm and 40 cm) for various treatment times (1, 2, 3, 5 and 10 minutes). Immediately after treatment, 10 µl of 216 mM PBS is added to stop the

conversion of nitrites into nitrates in acidic medium. 10 µl of sodium pyruvate is added to scavenge any possible traces of H_2O_2, as it might affect the Griess assay. 100 µl from each of the treated sample is extracted and added with 20 µl of Griess reagent with (conversion of nitrate to nitrite for quantifying the gross nitrite concentration) or without (for nitrite concentration) addition of 80 µl of VCl_3 solution.

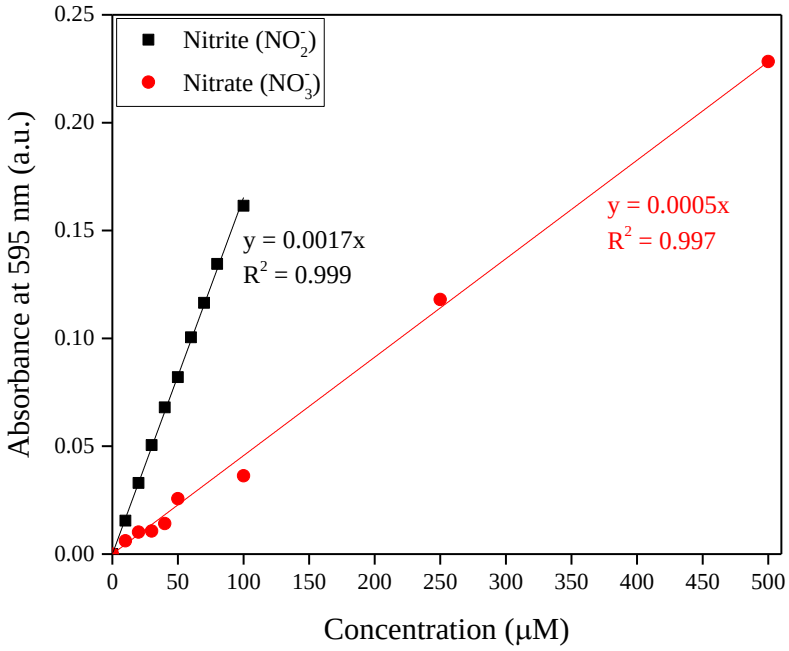

Figure 3.2. Nitrite and nitrate calibration curves. Nitrite standards (10-100 µM) after 30 minutes incubation at room temperature, and nitrate standards (10-500 µM) after 30 minutes incubation at 37^{0}C and 5% CO_2. The equation of the calibration curves and corresponding R-squared values are also shown.

A photometric reference sample (control) is prepared by mixing 20 µl of Griess reagent and 180 µl of deionized water for nitrite, and an additional 80 µl of VCl_3 for nitrate measurement. After 30 minutes of incubation at room temperature for nitrite and 37^{0}C for nitrate measurement, the absorbance is measured by a microtiter plate (MR) reader (E Max MR, Molecular Devices, Sunnyvale CA) at 595 nm relative to the photometric

reference sample. The absorbance values are converted to nitrite and nitrate concentrations by using the nitrite and nitrate calibration curves as shown in Figure 2.

3.3. Results and Discussions

3.3.1. Gas-phase treatment

3.3.1.a. Parameter dependence

Figure 3.3 shows the reduction in FCV titer as a function of treatment time for different powers, but without the use of an enclosure around the platform. It is clear that full inactivation can be achieved at higher power and within 4 minutes. All experiments from here onwards are done with an added enclosure to avoid diffusion of reactive species produced by plasma into the surrounding air. The effect of flow rate and exposure distance on virucidal inactivation is found to be minimal (not shown here). Based on these initial results, the plasma operating conditions are fixed at a flow rate of 16.4 slm and discharge power of 14.5 W. The maximum increase in gas temperature for this condition can be estimated assuming that all heat is removed through forced convection by the gas flow:

$$\Delta T = \frac{P}{\dot{m} C_p \rho} \approx 43\text{K} \tag{3.1}$$

An exposure of the virus samples to a gas flow at 325 K for 4 minutes does not lead to any inactivation as samples at the closest distance are not activated in dry conditions (see further).

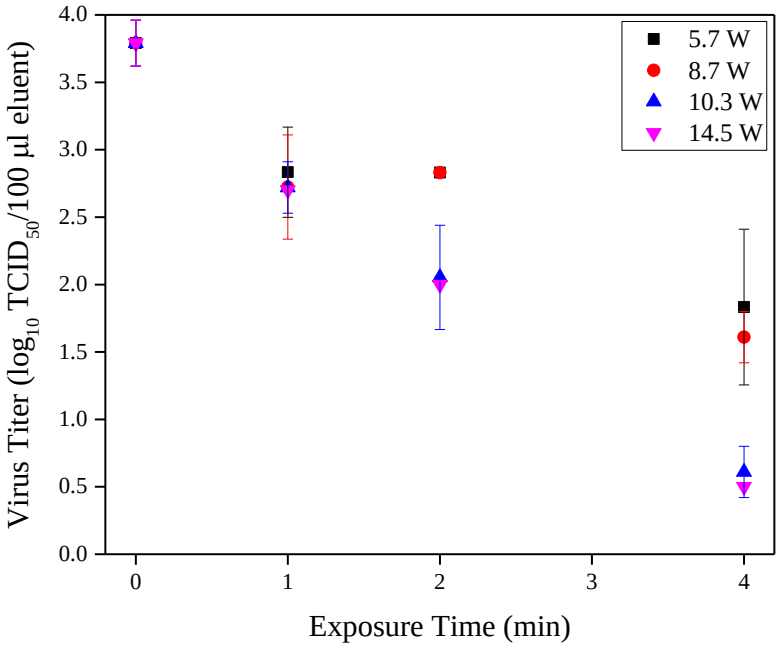

Figure 3.3. Effects of discharge power and treatment time on FCV titer at 10 slm and 3 mm exposure distance.

3.3.1.b. Effect of humidity

The effect of humidity on virucidal activity for the surface disinfection in the gas phase is shown in Figure 3.4. There is a negligible reduction in the virus titer for dry samples, while significant inactivation is seen for wet samples within minutes of exposure. This result is consistent with the findings of Hudson *et al*, in which an increased reduction in virus titer is observed for increase in added humidity to the sample during ozonizer treatments [55]. However the results shown by Hudson *et al* show that both dry and wet bacteria samples are equally affected by ozone [60], suggesting the effect might be virus or even species specific.

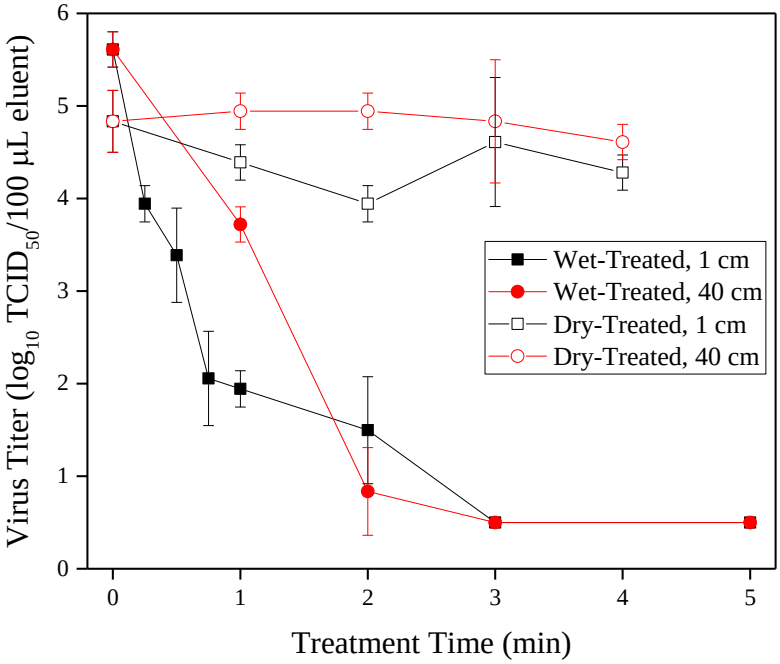

Figure 3.4. Wet and dry treatment of FCV-coated steel discs at 14.5 W and 16.4 slm air flow rate 1 cm and 40 cm from the discharge as a function of treatment time. Discs are sprayed with distilled water every 2 minutes in between treatment starting at 0 minute.

3.3.1.c. Assessment of underlying inactivation mechanism

Figure 3.5 shows that a close to complete inactivation of FCV (>4log$_{10}$ TCID$_{50}$/100µl) is achieved even for a treatment distance of 40 cm. This suggests that long-lived species are responsible for the suppression of virucidal activity. The most abundant long-lived species produced by DBDs in dry air are singlet oxygen, O_3, N_2O, NO_2 and N_2O_5 [26]. For the typical discharge conditions, the N_2O density is higher than the NO_2 and N_2O_5 density [26], although mainly NO_2 is suggested to have microbicidal effects [50]. Singlet oxygen ($O_2(a\ ^1\Delta_g)$) has been shown to be important in the inactivation of FCV for Ar RF driven plasma jets [4]. However the $O_2(a\ ^1\Delta_g)$ density was below the detection limit of 4×10^{19} m^{-3} for the plasma conditions used for the virus inactivation. The virus treatments using the microdischarge array are performed with a minimum gas residence time, t_{res} of 0.283 s at 5 mm from the discharge, which means that the highest $O_2(a\ ^1\Delta_g)$ density for

the treatment conditions is at most 37% of the detection limit. The $O_2(a\ ^1\Delta_g)$ density is 3 orders of magnitude smaller than the ozone density (see also further) and it can be concluded that $O_2(a\ ^1\Delta_g)$ will not be the dominant species responsible for the virus treatment.

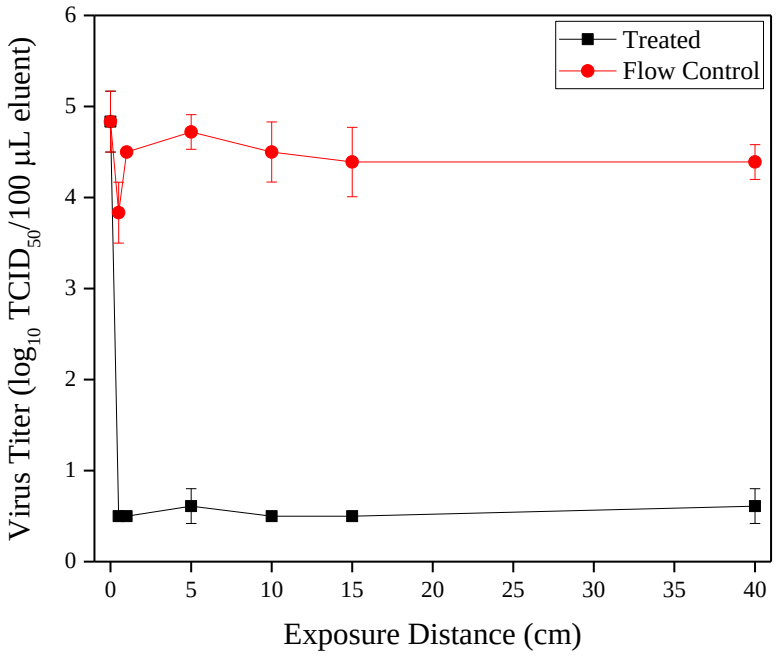

Figure 3.5. Plasma treatment of wet FCV-coated steel discs at 14.5 W and 16.4 slm air flow rate for 5 minutes as a function of exposure distance from the discharge. Discs are sprayed with distilled water every 2 minutes in between treatment starting at the start of the plasma treatment.

Ozone has been widely used for liquid treatment, but is less effective for surface disinfection of bacteria [50]. The measured ozone density in the surface DBD batch reactor of Graves *et al* [5] decreases with power density (> 0.20 W/cm2) because of the higher NO_x production and accumulation, leading to O_3 quenching. Figure 3.6 shows that the O_3 concentration keeps increasing with power up to 12 W (corresponding to a power density of 48.8 W/cm^2) and saturates at higher powers. However the HNO_3 concentration captured from the effluent gas when bubbling through a liquid is also the highest for the highest powers.

In order to compare the production of O_3 and NO_x, the plasma-treated effluent at same plasma operating conditions is bubbled through a gas washing bottle containing 150 ml of sterile DW. Figure 3.6 shows the nitrates concentration as a function of power and Figure 3.7 shows the concentration of nitrites and nitrates measured as a function of treatment time. The linear increase suggests that the concentrations can be used as a measure for the production of NO_3^-. The nitrite and nitrate concentrations are determined as described in *Section 3.2.7*. These species can be formed by the discharge via reactions in the liquid phase as shown below [52] –

$$NO_2 + NO_2 + H_2O \rightarrow NO_2^- + NO_3^- + 2H^+ \quad (3.2)$$

$$NO_2^- + O_3 \rightarrow NO_3^- + O_2 \quad (3.3)$$

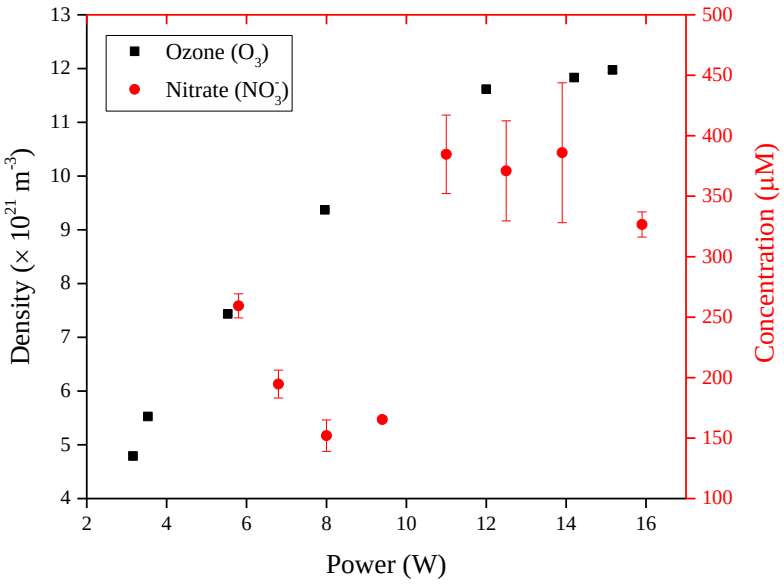

Figure 3.6. Absolute ozone [O_3] density in the gas phase and HNO_3 density in the liquid phase through which the effluent is bubbled as a function of discharge power.

Negligible amount of nitrites is measured, while the nitrate concentration increases linearly with treatment time. This might be due to the rapid reaction of NO_2^- with O_3 as

shown in the reaction above. Although nitrites are known to be effective against microbes in surface treatment [50], this is not likely from the small nitrite concentration shown in Figure 3.7. Figure 3.6 clearly shows that the higher power conditions also correspond with a higher concentration of NO_3^- and thus NO_2 in the gas phase. The production rates of O_3 and NO_3^- are 3.22×10^{18} molecules s^{-1} and 2.73×10^{18} molecules s^{-1}, respectively. As the conversion of NO_2 into NO_3^- is not complete and because of Henry's Law accounting for mixing into liquid phase, the NO_x concentration will be more than that of NO_3^- in liquid phase, which suggests similar or even higher production rate of NO_x compared to O_3. This higher NO_3^- concentration seems to correlate for the powers where O_3 saturates.

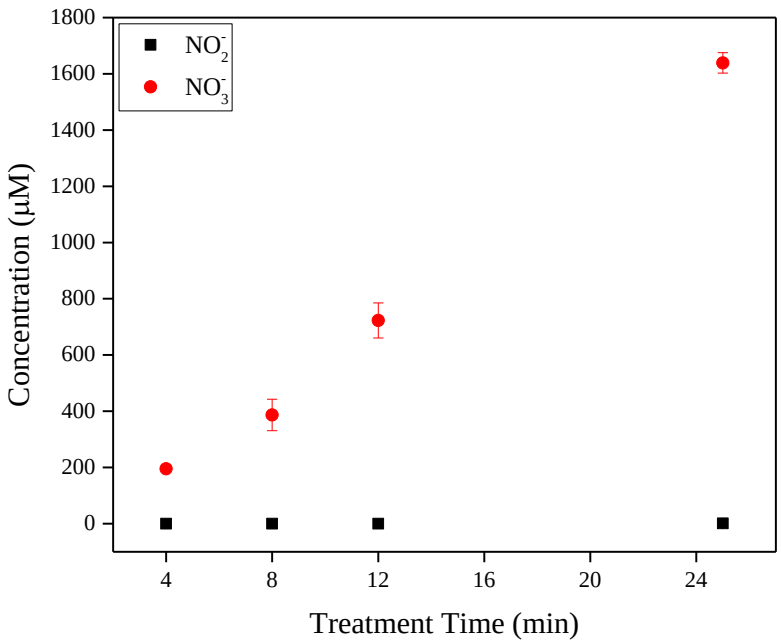

Figure 3.7. Nitrite (NO_2^-) and nitrate (NO_3^-) concentration measurement in DI water bubbler as a function of discharge treatment time.

It has been shown that > $2.9\log_{10}$ reduction in virus titer is achieved for surface treatment of FCV by only ozone treatment (20 ppm for 20 minutes) at 70% RH [55]. The O_3 produced in this work is almost 6 times higher with a contact time of 5 minutes which

leads to comparable Ct values (product of concentration disinfectant and contact time). This suggests that the measured ozone concentration is sufficient for inactivation of FCV. While O_3 is reported to be more effective in wet conditions, it is, however, unclear why in this case O_3 inactivation of a wet sample would lead to a more effective inactivation.

3.3.2. Liquid-phase treatment

In order to further investigate the improved inactivation of wet samples, suspended aliquots of virus in buffered liquid solution, NaCl-Tris-EDTA (NTE pH 7.4) are exposed to plasma and treated for various times. The results are shown in Figure 3.8. A significant reduction in FCV titer (>3$\log_{10}$ $TCID_{50}$/100 µl) is observed for only 1 cm exposure distance and 10 minutes of treatment. No swirling action is observed during the treatment, neither the treated sample is vortexed post-treatment. The lack of inactivation at 40 cm is consistent with the results of Graves that showed that for efficient inactivation of pathogens in solution by ozone, the mass transfer of ozone from the gas to the liquid phase needs to be enhanced by vortexing of the liquid sample [5].

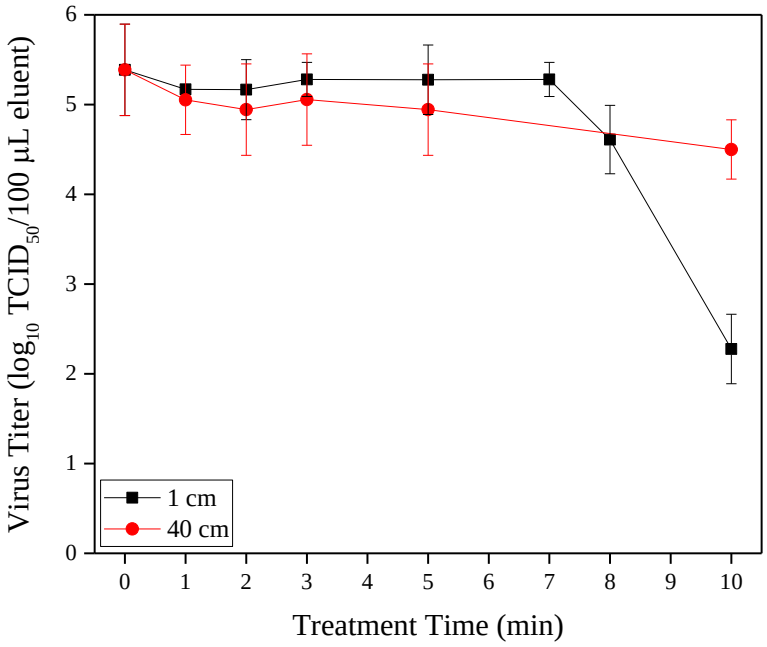

Figure 3.8. Treatment of FCV in NaCl-Tris-EDTA (NTE) buffer solution as a function of time at 14.5 W, 16.4 slm, and 1 cm and 40 cm from the discharge.

3.3.2.a. Assessment of underlying inactivation mechanism

The liquid-phase concentration of ozone can be estimated by using the gas-phase O_3 concentration and Henry's law constant of 0.013 mol kg^{-1} bar^{-1} assuming equilibrium between gas and liquid phases [61]. The aqueous ozone concentration is estimated to be 0.30 mg/l, which is more than the Ct values (<0.01 – 0.03 mg/l/min) reported in [54] for inactivation of virus in liquid medium. This suggests that the equilibrium of ozone concentration between the gas and the liquid phases is not achieved and the antiviral activity is mass-transfer limited.

A plot of the pH of treated liquid (sterile DW and NTE) as a function of treatment time is shown in Figure 3.9. Interestingly, a large drop in pH for the treated sample at 1 cm is observed even for a buffered solution of NTE (see Figure 3.9). The results for distilled

water show also that the drop in pH is larger for the sample at 1 cm than at 10 cm suggesting more RNS is transferred to the liquid close to the discharge.

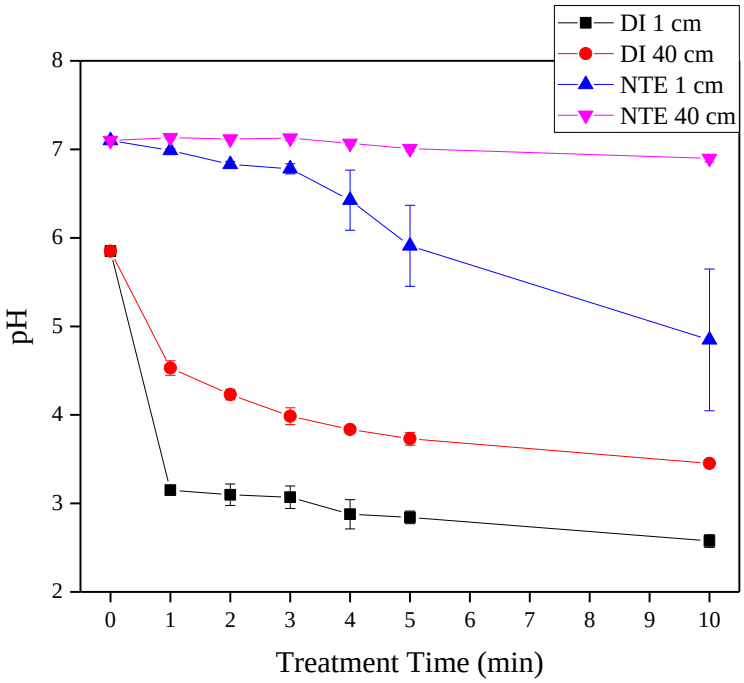

Figure 3.9. pH measurement of treated distilled water (DI) and NTE solution at 1 cm and 40 cm from discharge as a function of time.

In order to assess the lifetime of the reactive species responsible for virus inactivation, the virucidal effects of plasma treated distilled water and NTE buffered solution are assessed at different times after plasma treatment as shown in Figure 3.10. As no inactivation is observed for in the indirect treatment for plasma activated water with a delay of 0 minute, it suggests that short lived species such as acidified nitrates or peroxynitrite chemistry is involved. Aboubakr *et al* show from time delay measurements that both O_3 and NO_2^- are responsible for FCV inactivation up to several minutes after the treatment [4].

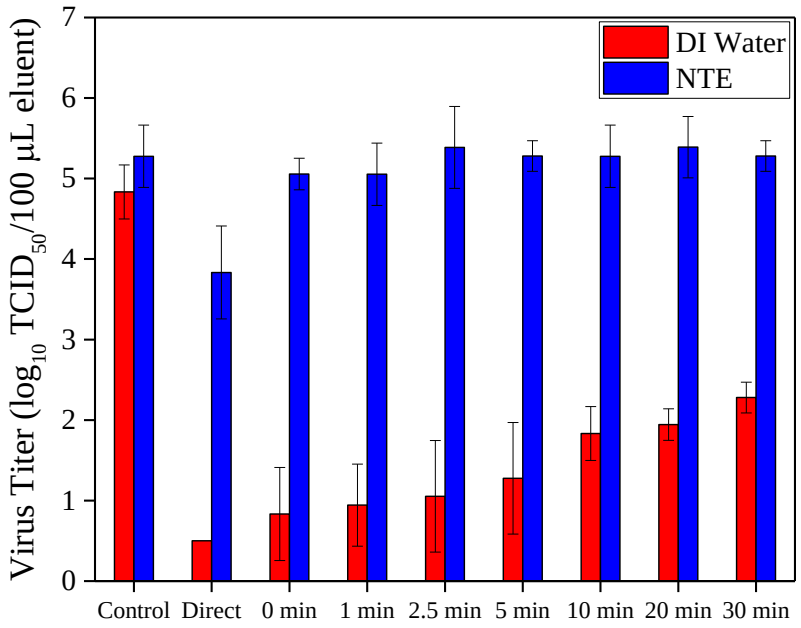

Figure 3.10. FCV inactivation of plasma treated distilled water at 14.5 W and 16.4 slm for 10 minutes and 1 cm exposure. Virus is added to the DI water and NTE before the treatment (Direct) and at various delay times after the treatment. Unexposed virus solution is the Control.

The nitrites and nitrates concentrations for 1 cm and 40 cm exposure distances at various treatment times is shown in Figure 3.11. For a treatment time of 10 minutes, the NO_2^- concentration in liquid phase is measured to be 33 µM. This is equal to 1.55 mg/l and is 5 times larger than the O_3 concentration in liquid. Aboubakr *et al* show by positive control experiments of $NaNO_2$ and H_2O_2 mixtures at reduced pH that a synergetic effect of peroxynitrite chemistry or acidified nitrites can be responsible for FCV inactivation in liquid medium [4]. However the concentration of NO_2^- was 1 mM to achieve 1 log reduction in virus titer. This suggests that other intermediate species such as NO_2 might play a role. The correlation between RNS transfer to the liquid, pH and virus inactivation for 1 and 40 cm suggests that NO_x species play a role in virucidal inactivation in liquid-phase treatment.

The importance of RNS in the liquid phase treatment could suggest that both ROS and RNS might have similar production (see higher), which might be related to the necessity of wetting the surface. Indeed the formation of peroxynitrous acid or acidified nitrates will be made possible by the presence of a liquid phase and improve the inactivation efficiency. This suggests that in a flow through reactor the combined interaction of RNS and O_3 might be much more significant than in a batch reactor as studied by Graves *et al* who found two distinctive inactivation modes based on O_3 and NO_x [5]. It is however important to note that different sensitivities can exist for virus and bacteria used in both studies.

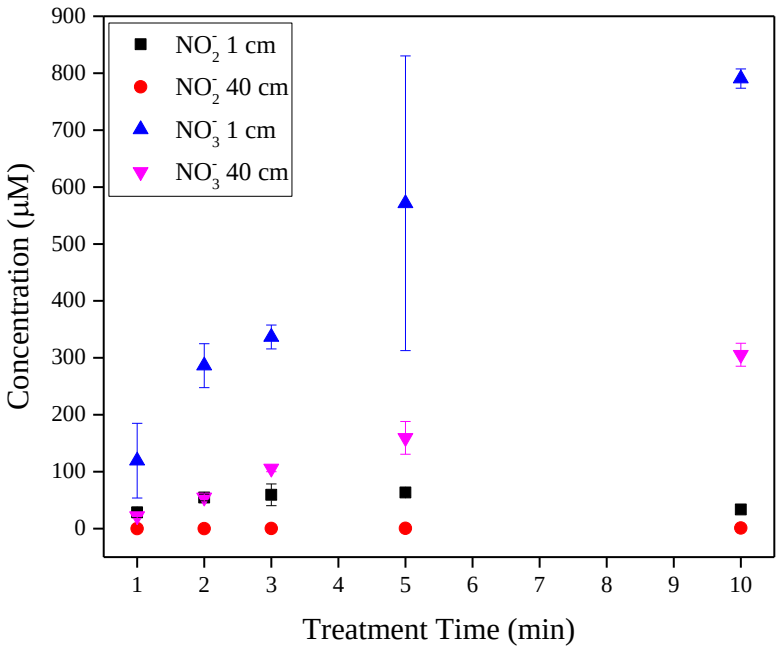

Figure 3.11. Nitrite (NO_2^-) and nitrate (NO_3^-) concentration measurement at 16.4 slm and 14.5 W.

3.4. Conclusion

The present work investigated the surface inactivation of virus in the gas-phase and virus suspensions by an array of microdischarges operated in air at atmospheric pressure at

various operation conditions (power, flow, exposure time and distance). Opposed to the trend of ozone production by the batch reactor [5], the discharge source in the flow-through reactor creates an increasing concentration of ozone with increasing power in the investigated power range. The increase in NO_x coincides with the increase in ozone at higher powers. It is shown that a higher degree of virucidal activity is achieved for the treatment of wet surface samples. The surface treatment is also independent of the exposure distance from the plasma (up to 40 cm) indicating that long-lived species are responsible for inactivation in the gas-phase. The Ct values for ozone in our reactor that lead to inactivation are consistent with inactivation for a reported ozonizer study.

The inactivation of virus in liquid phase is less effective suggesting that the inactivation is mass-transfer limited. The plasma treated liquid is only virucidal for less than 1 minute, showing the importance of short-lived species in liquid-phase treatment. It is also shown that lower pH affects the virus titer in liquid medium and a correlation between NO_2^- and NO_3^- concentrations in the liquid phase with virus inactivation suggest the importance of RNS for liquid treatment.

Finally, it should be emphasized that different reactors give rise to their own chemical inactivation pathways. For instance, plasma jets cause convection in liquid resulting into enhanced mixing and species transfer from the gas to the liquid phase. A batch reactor typically does not have a convective flow and in addition leads to the accumulation of NO_x that can cause ozone poisoning. However, this is not the case in the flow-through reactor studied in this chapter, for which both RNS and ROS can be involved in virus inactivation for the same plasma conditions.

Conclusion

The objective of this work was to characterize a dielectric barrier discharge source operating in air at atmospheric pressure and different flow rates, to determine the production and evolution of species and to assess the inactivation of Feline Calicivirus (FCV), a surrogate of human norovirus by the plasma source. A two-dimensional array of microdischarges is investigated allowing for a gas flow through the discharge zone with a minimum gas residence time equal to the discharge period. The plasma source has been subjected to several diagnostics such as current voltage measurements for electrical characterization and power measurements, optical emission spectroscopy (OES) to determine the gas temperature, CCS for microdischarge evolution and timescales, UV absorption spectroscopy to measure the O_3 density, absolute IR OES to measure the $O_2(a\ ^1\Delta_g)$ density and spectrophotometry to estimate the NO_x species density in aqueous medium. The plasma source is used to treat FCV in both gas and liquid phases. The following paragraphs summarize the key results.

The electrical characterization of the microdischarge array shows a unique structure of the voltage-charge plot with elongated sections, which define the dark periods or no discharge zones during part of the voltage waveform. The temperature difference for the investigated conditions in this study varies by not more than 50 K, which is lower than required for FCV inactivation by heating alone. Highly time-resolved cross-correlation spectroscopic measurements have been performed on a single microdischarge geometry, which provides detailed information about some specific emission in air plasma like NO_γ, SPS and FNS. The NO density is found to be reducing with smaller gas residence time,

showing a very strong effect of flow on the NO density. The most striking feature of this diagnostics has been the provision for estimation of the electric field by the ratio of intensities of SPS and FNS transitions. The reduced electric field, E/N in the discharge filament appears to be dependent on the flow rate. The space-charge distribution strongly depends on the flow rate and could be due to a change in humidity and a reduction of pre-ionization by the gas flow.

It has been previously reported that singlet delta oxygen ($O_2(a\ ^1\Delta_g)$) plays a major role in FCV inactivation. We measured for the first time the absolute densities of $O_2(a\ ^1\Delta_g)$ in a DBD in dry air by IR emission in this work. The density is highly affected by the residence time in the afterglow. A maximum density (in the discharge zone) of 10^{22} m^{-3} is achieved at an intermediate flow rate of 20 slm, while at higher flow rate and similar discharge power, it reduces by almost 50%. This is explained with a variation in the gas residence time in the discharge region that leads to a dilution of the singlet oxygen density. An optimal condition for singlet oxygen generation is found that is a balance between power and gas residence time. For this condition, the effect of the accumulative singlet oxygen density by multiple discharge events is ideally complemented with a minimum in quenching. A higher power or residence time would in this case lead to a higher concentration of quenchers or longer exposure to the quenchers leading to a further reduction of the singlet oxygen density. Also it is found that the $O_2(a\ ^1\Delta_g)$ to O_3 density ratio in the afterglow can be controlled by the flow rate from 0.7 to approximately 0. However, at the conditions used for inactivation of FCV, no $O_2(a\ ^1\Delta_g)$ could be

measured, suggesting that it is not important for the virucidal effect for this particular source.

The discharge source is used for treating FCV in both gas and liquid phase. We have found that both O_3 and NO_x increase with discharge power. A comparison of virus inactivation shows that wet samples are more effectively inactivated than the dry samples in gas phase. The results indicate that long-lived species are responsible for the inactivation. The measured ozone concentration seems to be sufficient to inactive the virus in the gas phase based on comparison of Ct values with other published studies. It is also found that the inactivation seems mass-transfer limited in solution, and short-lived species are important for the inactivation of virus in aqueous suspensions. The pH of the solution correlates with the virucidal effect, which combined with RNS measurements in the liquid phase, suggests that RNS are responsible for virucidal inactivity in liquid medium. The results suggest that in this flow through reactor a synergistic effect of both ROS and RNS (even in the gas phase) might be important. This is very different from results reported in a batch reactor where ozone poisoning by NO_x in the gas volume at long exposure times leads to two distinctive inactivation regimes based on O_3 and NO_x for different plasma powers.

Bibliography

[1] von Woedtke T, Metelmann H-R and Welmann K-D 2014 Clinical plasma medicine: state and perspectives of *in Vivo* application of cold atmospheric plasma *Contrib. Plasma Phys.* **54** 2 104 – 117

[2] Graves D B 2014 Low temperature plasma biomedicine: a tutorial review *Phys. Plasmas* **21** 080901

[3] Julák J, Scholtz V, Kotúčová S and Janoušková O 2012 The persistent microbicidal effect in water exposed to the corona discharge *Physica Medica* **28** 230-239

[4] Aboubakr H A, Gangal U, Youssef M M, Goyal S M and Bruggeman P J 2016 Inactivation of virus in solution by cold atmospheric pressure plasma: identification of chemical inactivation pathways *J. Phys. D: Appl. Phys.* **49** 204001

[5] Pavlovich M J, Chang H-W, Sakiyama Y, Clark D S and Graves D B 2013 Ozone correlates with antibacterial effects from indirect air dielectric barrier discharge treatment of water *J. Phys. D: Appl. Phys.* **46** 145202

[6] Graves D B 2012 The emerging role of reactive oxygen and nitrogen species in redox biology and some implications for plasma applications to medicine and biology *J. Phys. D: Appl. Phys.* **45** 263001

[7] Aboubakr H A, Williams P, Gangal U, Youssef M M, El-Sohaimy S A A, Bruggeman P J and Goyal S M 2015 Virucidal effect of cold atmospheric gaseous plasma on feline calicivirus, a surrogate for human norovirus *Appl. Environ Microbiol* **81** 3612–3622

[8] Doležalová E, Prukner V, Lukeš P and Šimek M 2016 Stress response of Escherichia coli induced by surface streamer discharge in humid air *J. Phys. D: Appl. Phys.* **49** 075401

[9] Jeong J, Kim J Y and Yoon J 2006 The role of reactive oxygen species in the electrochemical inactivation of microorganisms *Environ. Sci. Technol.* **40** 6117–6122

[10] Sakai O, Kishimoto Y and Tachibana K 2005 Integrated coaxial-hollow micro dielectric-barrier-discharges for a large-area plasma source operating at around atmospheric pressure *J. Phys. D: Appl. Phys.* **38** 431-441

[11] Höft H, Becker M M and Kettlitz M 2016 Impact of gas flow rate on breakdown of filamentary dielectric barrier discharges *Physics of Plasmas* **23** 033504

[12] Moreau E 2007 Airflow control by non-thermal plasma actuators *J. Phys. D: Appl. Phys.* **40** 605-636

[13] Akishev Y, Goossens O, Callebaut T, Leys C, Napartovich A and Trushkin N 2001 The influence of electrode geometry and gas flow on corona-to-glow and glow-to-spark threshold currents in air *J. Phys. D: Appl. Phys.* **34** 2875-2882

[14] Ashpis D E, Laun M C and Griebeler E L 2012 Progress toward accurate measurements of power consumptions of DBD plasma actuators *50th Aerospace Sciences Meeting*

[15] Bruggeman P J, Sadeghi N, Schram D C and Linss V 2014 Gas temperature determination from rotational lines in non-equilibrium plasmas: a review *Plasma Sources Sci. Technol.* **23** 023001

[16] Laux C O, Spence T G, Kruger C H and Zare R N 2002 Optical diagnostics of atmospheric pressure air plasmas *Plasma Sources Sci. Technol.* **12** 125–138

[17] Kozlov K V, Wagner H-E, Brandenburg R and Michel P 2001 Spatio-temporally resolved spectroscopic diagnostics of the barrier discharge in air at atmospheric pressure *J. Phys. D: Appl. Phys.* **34** 3164-76

[18] Hoder T, Cernak M, Hoft H, Gerling T and Brandenburg R 2015 Time-correlated single photon counting spectroscopy: Principles and applications to single-filament discharges *Proceedings of Science*

[19] Paris P, Aints M, Valk F, Plank T, Haljaste A, Kozlov K V and Wagner H-E 2005 Intensity ratio of spectral bands of nitrogen as a measure of electric field strength in plasmas *J. Phys. D: Appl. Phys.* **38** 3894-99

[20] Manley T C 1943 The electric characteristics of the ozonator discharge *Trans. Electrochem. Soc.* **84** 1

[21] Itikawa Y 2006 Cross sections for electron collisions with nitrogen molecules *J. Phys. Chem. Ref. Data* 35 31

[22] Bacri J and Medani A 1982 Electron diatomic molecule weighted total cross section calculation *Physica* **112C** 101-118

[23] Simek M, Prukner V and Schmidt J 2011 Optical and electrical characteristics of a single surface DBD micro-discharge produced in atmospheric-pressure nitrogen and synthetic air *Plasma Sources Sci. Technol.* **20** 025009

[24] Herron J T and Green D S 2000 Chemical kinetics database and predictive schemes for non-thermal humid air plasma chemistry *Plasma Chemistry and Plasma Processing* **21** No. 3

[25] De Benedictis S, Dilecce G and Simek M 1997 The NO($A\ ^2\Sigma^+$) excitation mechanism in a N_2–O_2 pulsed RF discharge *J. Phys. D: Appl. Phys.* **30** 2887–2894

[26] Eliasson B and Kogelschatz U 1991 Modeling and applications of silent discharge plasmas *IEEE Transactions on Plasma Science* Vol. **19**, No. 2

[27] Hoder T, Šíra M, Kozlov K V and Wagner H-E 2008 Investigation of the coplanar barrier discharge in synthetic air at atmospheric pressure by cross-correlation spectroscopy *J. Phys. D: Appl. Phys.* **41** 035212

[28] Pai D Z, Lacoste D A and Laux C O 2010 Nanosecond repetitively pulsed discharges in air at atmospheric pressure – the spark regime *Plasma Sources Sci. Technol.* **19** 065015

[29] Mintoussov E I, Pendleton S J, Gerbault F G, Popov N A and Starikovskaia S M 2011 Fast gas heating in nitrogen–oxygen discharge plasma: II. Energy exchange in the afterglow of a volume nanosecond discharge at moderate pressures *J. Phys. D: Appl. Phys.* **44** 285202

[30] Schulz G J 1962 Cross sections and electron affinity for O^- ions from O_2, CO, and CO_2 by electron impact *Physical Review* **128** 1

[31] Rapp D and Briglia D D 1965 Total cross sections for ionization and attachment in gases by electron impact. II. Negative-ion formation *J. Chem. Phys.* **43** 1480

[32] Matejcik S, Kiendler A, Cicman P, Skalny J, Stampfli P, Illenberger E, Chu Y, Stamatovich A and Mark T D 1996 Electron attachment to molecules and clusters of atmospheric relevance: oxygen and ozone *Plasma Sources Sci. Technol.* **6** 140–146

[33] Itikawa Y and Mason N 2005 Cross sections for electron collisions with water molecules *J. Phys. Chem. Ref. Data* **34** 1

[34] Ryżko H 1964 Drift velocity of electrons and ions in dry and humid air and in water vapour *Proc. Phys. Soc.* **85**

[35] Liu Y, Huang S and Zhu L 2015 Influence of humidity and air pressure on the ion mobility based on drift tube method *CSEE Journal of Power and Energy Systems* **Vol. 1** No. 3

[36] Ionin A A, Kochetov I V, Napartovich A P and Yuryshev N N 2007 Physics and engineering of singlet delta oxygen production in low-temperature plasma *J. Phys. D: Appl. Phys.* **40** R25–R61

[37] Samukawa S, Hori M, Rauf S *et al* 2012 The 2012 Plasma Roadmap *J. Phys. D: Appl. Phys.* **45** 253001

[38] Wieshaupt K R, Gomer C J and Dougherty T J 1976 Identification of singlet oxygen as the cytotoxic agent in photo-inactivation of a Murine tumor *Cancer Res.* **36** 2326–2329

[39] Panjehpour M, Overholt B F, Phan M N and Haydek J M 2005 Optimization of light dosimetry for photodynamic therapy of Barrett's esophagus: efficacy vs. incidence of stricture after treatment *Gastrointest. Endosc*. **61** 13–18

[40] Lowke J J 1992 Theory of electrical breakdown in air – the role of metastable oxygen molecules *J. Phys. D: Appl. Phys*. **25** 202-210

[41] Lebedev A V, Deminsky M A, Zaitzevsky A V and Potapkin B V 2013 Effect of $O_2(a\ ^1\Delta_g)$ on the low-temperature mechanism of CH_4 oxidation *Combust. Flame* **160** 530-538

[42] Smirnov V V, Stelmakh O M, Fabelinsky V I, Kozlov D N, Starik A M and Titova N S 2008 On the influence of electronically excited oxygen molecules on combustion of hydrogen–oxygen mixture *J. Phys. D: Appl. Phys.* **41** 192001

[43] Ombrello T, Wona S H, Ju Y and Williams S 2010 Flame propagation enhancement by plasma excitation of oxygen. Part II: Effects of $O_2(a\ ^1\Delta_g)$ *Combust. Flame* **157** 1916-1928

[44] Nagaraja S, Yang V and Adamovich I 2013 Multi-scale modelling of pulsed nanosecond dielectric barrier plasma discharges in plane-to-plane geometry *J. Phys. D: Appl. Phys.* **46** 155205

[45] Sousa J S and Puech V 2013 Diagnostics of reactive oxygen species produced by microplasmas *J. Phys. D: Appl. Phys.* **46** 464005

[46] Wu Y, Zhang Z and Ombrello T M 2013 Spatially resolved measurement of singlet delta oxygen by radar resonance-enhanced multiphoton ionization *Optical Letters* **38** 13

[47] Zhang S, van Gaens W, van Gessel B, Hofmann S, van Veldhuzien E, Bogaerts A and Bruggeman P 2013 Spatially resolved ozone densities and gas temperature in a time modulated RF driven atmospheric pressure plasma jet: an analysis of the production and destruction mechanisms *J. Phys. D: Appl. Phys.* **46** 205202

[48] Bauville G, Lacour B, Magne L, Puech V, Boeuf J P, Munoz-Serrano E and Pitchford L C 2007 Singlet oxygen production in a microcathode sustained discharge *Appl. Phys. Lett.* **90** 031501

[49] Bowman S S, Adamovich I V and Lempert W R 2014 Experimental and modeling analysis of singlet delta oxygen kinetics in a repetitively pulsed nanosecond discharge *Plasma Sources Sci. Technol.* **23** 035009

[50] Pavlovich M J, Clark D S and Graves D B 2014 Quantification of air plasma chemistry for surface disinfection *Plasma Sources Sci. Technol.* **23** 065036

[51] Zimmermann J L, Dumler K, Shimizu T, Morfill G E, Wolf A, Boxhammer V, Schlegel J, Gansbacher B and Anton M 2011 Effects of cold atmospheric plasmas on adenoviruses in solution *J. Phys. D: Appl. Phys.* **44** 505201

[52] Doležalová E, Prukner V, Lukeš P and Šimek M 2016 Stress response of Escherichia coli induced by surface streamer discharge in humid air *J. Phys. D: Appl. Phys.* **49** 075401

[53] Jeong J, Kim J Y and Yoon J 2006 The role of reactive oxygen species in the electrochemical inactivation of microorganisms *Environ. Sci. Technol.* **40** 6117–6122

[54] Lukes P, Dolezalova E, Sisrova I and Clupek M 2014 Aqueous-phase chemistry and bactericidal effects from an air discharge plasma in contact with water: evidence for the formation of peroxynitrite through a pseudo-second-order post-discharge reaction of H_2O_2 and HNO_2 *Plasma Sources Sci. Technol.* **23** 1

[55] Hudson J B, Sharma M and Vimalanathan S 2009 Development of a practical method for using ozone gas as a virus decontaminating agent *Ozone: Science & Engineering* **31** 3 216-223

[56] Hudson J B, Sharma M and Petric M 2007 Inactivation of Norovirus by ozone gas in conditions relevant to healthcare *J. Hosp. Infect.* 1-6

[57] Wink D A, Hines H B, Cheng R Y S, Switzer C H, Flores-Santana W, Vitek M P, Ridnour L A and Colton C A 2011 Nitric oxide and redox mechanisms in the immune response *J. Leukoc. Biol.* **89** 873–891

[58] Kärber G 1931 50% end point calculation *Arch. Exp. Pathol. Pharmacol.* **162** 480–483

[59] Miranda K M, Espey M G and Wink D A 2001 A rapid, simple spectrophotometric method for simultaneous detection of nitrate and nitrite *Nitric Oxide* **5** 1 62-71

[60] Sharma M and Hudson J B Ozone gas is an effective and practical antibacterial agent 2008 *American Journal of Infection Control* **36** 8

[61] Wilhelm E, Battino R and Wilcock R 1977 *Chem. Rev.* **77** 219-261